A novel flexible ultrasound neurostimulator featuring a pitch-matched 2D array

By

Hidde Woerdman

in partial fulfillment of the requirements for the degree of

Master of Science
in Biomedical Engineering

at the Delft University of Technology,
to be defended publicly on Wednesday, September 13, 2023 at 02:00 PM.

Supervisor:	Dr. T. Costa	TU Delft
Thesis committee:	Dr. A. Accardo	TU Delft
	Dr. T. Manzaneque	TU Delft

TU Delft

TU Delft
Delft University of Technology

A novel flexible ultrasound neurostimulator featuring a pitch-matched 2D PZT array

H.J. Woerdman *5419808*

***Abstract*— Ultrasound neurostimulation (UNS) is an emergent minimally-invasive neurostimulation (NS) modality employing focused ultrasound (US) waves. This technique enables sub-millimeter precision NS without invasive electrode implantation. However, existing commercial US transducers constrain UNS research due to their bulky form, inflexible substrate, and fixed focus. To enable subcranial brain stimulation in rats, there is a need for a miniaturized, flexible UNS. Flexible devices that were recently showcased had restrictions in terms of frequency and aperture, along with a non-optimal inter-element pitch. This study delves into microfabrication technology to expand the capabilities of flexible two-dimensional ultrasound phased arrays.**

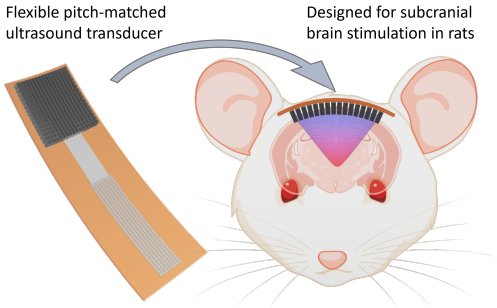

256 and 900-element 2D US transmitter arrays, designed to operate at 4 MHz with an inter-element pitch satisfying the criterion of half the wavelength, are presented. This pitch requirement is essential for optimal electronic beam-steering, preventing grating lobes (undesired maxima due to undersampling), and mitigating potential side effects. Three device variants operating at this frequency were developed: a fully flexible version housing a 16x16 transmitter array, an analogous variant but with a rigid contact pad array, and a fully flexible device with a 30x30 array. Fabrication employed an innovative microfabrication process alongside an optimized lead zirconium titanate (PZT)-integration technique. US characterization affirmed all devices' capacity to generate US waves, yielding planar waves with peak pressure outputs of about 140 kPa and 450 kPa for the 16x16 and 30x30 arrays, respectively.

This study introduces an innovative microfabrication approach that unites a flexible substrate with a pitch-matched 4 MHz PZT array—an unprecedented combination. These newly developed devices hold promise for advancing UNS research and expanding its potential applications.

I. Introduction

THE human brain is a complex and mysterious organ that has yet to be fully understood by the scientific community. Despite several decades of research and breakthroughs in neuroscience, we still have an incomplete understanding of the intricate workings of the brain that govern our thoughts, emotions, and behaviors [1]. Embedded within this complexity are disorders of the human brain. Brain disorders (BDs), including psychiatric diseases such as depression, schizophrenia, and obsessive-compulsive disorder, as well as neurological diseases like Alzheimer's disease, Parkinson's disease, epilepsy, and stroke, are major causes of disability and death worldwide [2], [3]. The treatment of BDs depends on the specific condition, but it often involves a combination of medical, therapeutic, and lifestyle interventions. While medications have been the cornerstone of treatment for many decades, they frequently lead to severe side effects and drug interactions. Moreover, 20-60% of patients with a BD suffer from treatment resistance [4]. Even though many aspects of BDs' causes and progressions remain unknown, substantial progress in brain research in the past decades has been made. For instance, it has been found that the brain can generate new neurons and restructure itself, a phenomenon referred to as neuroplasticity. This concept challenges the long-established view that the maximum amount of neurons is fixed after birth [1].

Neuroplasticity supports learning in the intact brain and functional improvement in the damaged or diseased nervous system [5]. While readily observable and measurable, these effects are difficult to control or manipulate intentionally [6]. Neurostimulation (NS) technologies provide an opportunity to harness the brain's plasticity and utilize this capability to understand the connection between different regions and networks and their functional connectivity patterns in relation to cognitive processes or symptoms of diseases. This technique encompasses implantable and non-implantable technologies with varying invasiveness to modulate brain function using electrical, magnetic, or other forms of energy. Neurostimulation can be accomplished through various techniques, including deep brain stimulation, transcranial magnetic stimulation, direct current stimulation, and focused ultrasound. Rather than relying on a single mechanism, NS is thought to exert its effects through a complex interplay of several mechanisms, including local and network-wide electrical and neurochemical effects of stimulation and modulation of brainwave activity and

plasticity [7]. The relative importance of these mechanisms varies depending on the condition being treated and the target being stimulated. In general, NS enables a more localized targeting of neurons than chemical medications since the medication is usually delivered to all neurons in the body by the bloodstream. However, the precise mechanisms by which NS works are not yet fully understood [8]. Insight into the technical basis of neurostimulation might be a first step towards a more profound understanding of these mechanisms, leading to improved clinical outcomes and therapeutic potential [9].

Ultrasound neurostimulation (UNS) is an emerging form of minimally invasive NS that utilizes focused ultrasound (US) waves. This technique enables neural modulation with submillimeter precision without requiring the invasive implantation of electrodes or other devices into the brain [10]. It has been shown to be effective and safe in various applications, including the treatment of neurological and psychiatric disorders, as well as the enhancement of cognitive function [10]. Several proposed mechanisms underlying the neurostimulatory effects of UNS are illustrated in Fig. 1. Recently, the mechanical interaction of US waves with the lipid membrane has received the most attention as a primary mechanism for NS. Ultrasound induces cell membrane deformation, leading to changes in membrane capacitance and channel kinetics, resulting in altered excitability [11]. However, further research is needed to fully understand these mechanisms and determine the optimal use of UNS in clinical settings [10]–[13]. Such research is currently being conducted *in vivo* and *in vitro*. Recent in-vivo experiments include animal studies in rats [14]–[18].

Ultrasound waves for UNS are produced using US transducers, which convert electrical energy into mechanical energy. A range of commercially available US transducers exists, differing in frequency, size, number of elements, and focal length. Generally, the current generation of commercial transducers can produce a high output pressure but have several limitations that hamper progress in UNS research. These limitations include the transducer's (1) bulky form factor, (2) rigid substrate resulting in non-flexible devices, and (3) non-adjustable focus.

Firstly, the limitations above combined result in non-wearable devices and stimulation in a dedicated facility by an operator, impeding free-moving and long time-duration experiments (Fig. 2). Secondly, because of the bulkiness and rigidity of the US transducers, these devices cannot be placed underneath the skull. This leaves transcranial (i.e., through the skull) US delivery as the only option. Transcranial UNS poses challenges, however, since the US waves suffer from attenuation and scattering due to the high acoustic mismatch between the skull bone and soft tissue. To reduce the attenuation/losses, studies on transcranial UNS are limited to low frequencies ($<$ 1MHz), leading to lower precision and a larger focal spot [14], [16], [17]. Another solution involves placing the transducer directly on the brain after a partial craniotomy (i.e., partial removal of the skull), which leaves the brain exposed and vulnerable [15]. Lastly, single-element transducers have a fixed focal point. The transducer must be physically moved or switched to change the location of the focal spot. Multiple

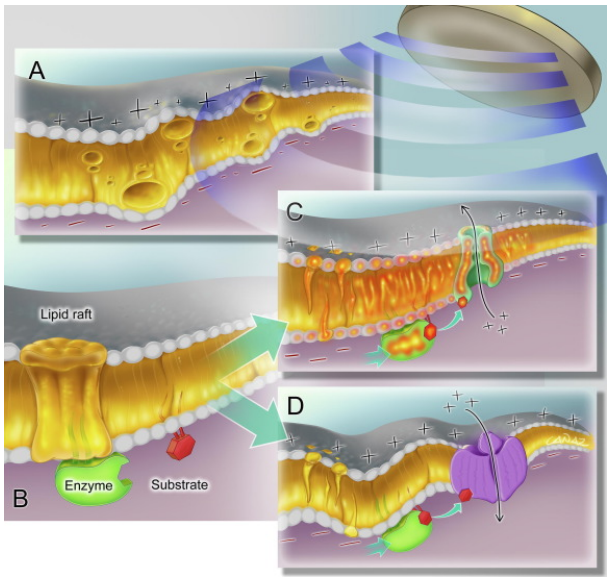

Fig. 1: Proposed mechanisms of ultrasound neurostimulation [11]. A: Acoustic cavitation causes the formation of bubbles inside the neuronal membrane, resulting in capacitance changes or fracture of the cell membrane. B: Lipid rafts segregate intracellular enzymes and limit interactions with membrane-bound substrates. C: Increased temperature or (D) mechanical force applied to the membrane disrupts these lipid rafts, resulting in translocation of the enzyme, increasing substrate enzymatic reactions. The molecules that emerge alter the ion channel gating, resulting in modulated excitability.

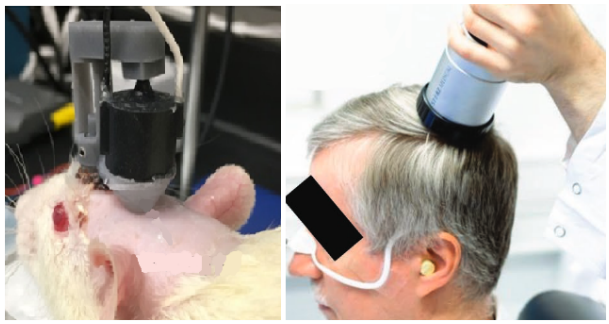

Fig. 2: Transcranial ultrasound neurostimulation using bulky transducers on a rat brain (left) [16] and a human brain (right) [19].

transducers with different characteristics are sometimes necessary to conduct experiments with different parameters, e.g., brain stimulation at different depths, increasing the costs and imposing risks.

Currently, the field is developing a new generation of US transducers to overcome the aforementioned shortcomings, enabling scientists to conduct new experiments and research. In this study, the design, fabrication, and US characterization of a novel flexible US transducer is presented. The device was intended for animal studies in rodents, especially on rat brains, and was designed according to the following requirements:

- **Miniturized form factor.** To enable UNS directly on the brain's cortex, the device must be miniaturized to be

implanted on the dura underneath the skull. By taking this approach, it becomes possible to circumvent the skull, resulting in decreased US attenuation and scattering, thus enabling the utilization of higher frequencies and achieving greater precision. To achieve this, the dimensions were limited to a maximum of 10 mm wide and 1.5 mm thick. For UNS in mid-brain regions, the transducer must be able to reach targets up to 8 mm from the transducer [20].

- **Flexible substrate.** Placing a miniaturized but rigid device in the sub-cranial space is still problematic because the brain and skull are not flat but curved. To accommodate a device within the sub-cranial region, it must be flexible to conform to the curvatures of the skull.
- **Electronic beam steering using a phased array.** To precisely stimulate specific targets within neural tissue, it is essential to steer the US beam in the appropriate direction and focus it into a small area known as the focal spot. In multi-element arrays, the beam and focal spot can be electronically focussed and steered by adjusting the delay of the excitation pulses for each individual element. Such an array capable of electronic beam steering is known as a "phased array" [21]. In a phased array, all elements must be individually addressed by interconnecting traces. A crucial design criterium is the inter-element pitch ((d), i.e., the center-to-center distance between two successive elements), which must be half of the US wavelength (λ) in soft tissue for adequate beamforming without grating lobes (i.e., additional maxima at unwanted locations due to under-sampling [22]), elaborated upon in section II-C.1).

The work presented here builds on recent efforts to realize miniaturized phased array transducers [22]–[26]. Two studies used a flexible printed circuit board (PCB) to create flexible US transducers. Using this technique, Ellaion et al. [25] realized a 1.4 MHz 256-element array with a 0.91 λ pitch, and Pashaei et al. [24] created a 1.3 MHz 64-element linear array at 0.65 λ pitch. Although multi-element flexible phased arrays were fabricated successfully, the pitch values are above optimal, and the frequencies are limited to below 1.5 MHz. Elloian et al. mention the pitch was limited due to PCB routing constraints, given the required number of interconnections to address all elements individually. A device by Hu et al. was operated at a higher frequency; they developed a stretchable 16x16 array driven at 3 MHz [23]. Using a laser ablation technique, multi-layer serpentine-shaped electrodes were fabricated, which enabled impressive stretchability of the array. However, this approach led to a pitch of 800 μm, more than 3 times the optimal value at that frequency. By relying on microfabrication technology, other researchers did succeed in creating phased arrays at optimal pitch. Seok et al. [26] integrated a 2 MHz 32x32 array on an application-specific integrated circuit(ASIC), and Costa et al. [22] reached an even higher frequency with a 10 MHz 26x26 array based on complementary metal oxide semiconductor (CMOS) technology.

In the aforementioned state-of-the-art fabrication processes, only microfabrication-based CMOS solutions achieved the combination of a high-frequency, big aperture, and pitch-matched array. However, because CMOS is based on a rigid silicon substrate, the applicability is limited when flexibility and high conformability are required. On the other hand, the flexible phased array solutions that were presented relied on either PCB or custom laser-ablation technologies, all suffering from fundamental limitations in terms of minimum feature size. Consequently, these devices exhibited restrictions in terms of frequency, aperture size, and possessed a pitch exceeding the minimum requirement. In this work, microfabrication technology is explored and used to push the boundaries of flexible two-dimensional US phased arrays towards a pitch-matched, high frequency, big aperture, flexible neurostimulator. The envisioned system comprises two parts: the front end and the back end. The front end is a passive, flexible US transducer. The back end is a commercial, computer-based US driver (Vantage 256, Verasonics) capable of driving a maximum of 256 elements. This article is focused on the design, fabrication, and US characterization of the front end. Devices housing 256 and 900 elements transducer elements, designed to be driven at 4 MHz, are presented.

II. Materials and Methods

A. Substrate and transducer materials

1) Flexible substrate: In recent attempts, both Polyimide (PI) [24], [25], [27] and polydimethylsiloxane (PDMS) [23] were used as flexible substrates for US transducers. PDMS is a significantly more elastic polymer than PI, with Young's moduli (YM) < 1.0 MPa versus $\approx 2-3$ GPa, respectively [28]. PDMS's low YM makes it stretchable to multiple times the original length, whereas PI is hardly stretchable at all [29]. For our application, the device must be flexible enough to conform to a small animal's skull; stretchability is unnecessary and undesirable since the strain posed on the interconnects necessitates a more complex serpentine-shaped design [23], [29], [30]. Here, PI was chosen as substrate material; PI is biocompatible, is available in photo-patternable formulations, can be deposited using spin-coating, and has high thermal stability of $300-400°C$ [29], [31]. This thermal stability enables high-temperature microfabrication techniques, such as plasma-enhanced chemical vapor deposition (PECVD), typically performed at $\geq 300°C$, something not possible with PDMS, which is thermally stable up to only $200°C$.

2) Ultrasound transducer elements: The most commonly used types of transducers in US phased arrays include bulk piezoelectric transducers, micromachined capacitive micromachined US transducers (cMUTs), and micromachined piezoelectric micromachined US transducers (pMUTs).

In bulk transducers, a piezoelectric material, typically lead zirconate titanate (PZT), is diced into smaller elements and integrated into a separately made device. Through the piezoelectric effect, the individual elements can be brought into vibration by an alternating electric field matching the resonance frequency (f_r). This electric field is generated through a signal and ground electrode, one on either side of the PZT element. f_r can be found following 1, where PZT_{th} is the

Transducer Type	Characteristics
Bulk	High transmit power
	Moderate receive sensitivity
	Low bandwidth
	Matching layer
	No DC-bias required
cMUT	Moderate transmit power
	High receive sensitivity
	High bandwidth
	No matching layer required
	High DC-bias required
pMUT	Moderate transmit power
	Moderate receive sensitivity
	Low bandwidth
	No matching layer required
	No DC-bias required

TABLE I: Qualitative comparison of the three most common ultrasound transducer types [32], [33].

thickness of the PZT element and c_P the acoustic propagation speed inside the piezoelectric material (≈4500 m/s in PZT).

$$f_r = \frac{c_P}{2PZT_{th}} \quad (1)$$

PZT has the highest quality factor (Q) and electroacoustic transmit sensitivity (S_{tx}) of all three types of transducers, of which the latter can be improved even further by applying a matching layer in front of the transducer to reduce reflections due to the high acoustic mismatch with soft tissue [22].

Both cMUTs and pMUTs, on the other hand, use an oscillating membrane spanned above a cavity to produce US waves. The vibration of this membrane is achieved by using capacitive (cMUT) or piezoelectric (pMUT) effects. The vibrating membrane entails efficient coupling to soft tissue, overcoming the necessity for a matching layer. However, S_tx is lower than PZT. Because pMUTs and CMUTs are made directly in a microfabrication process, they are generally considered more CMOS-compatible than PZT. A disadvantage for implantable devices is the high DC voltage required to bias the membrane in cMUTs.

Considering the most important characteristics of the different types of transducers (Table I, [32], [33]), the bulk PZT transducer was considered the most suitable option for our device. PZT enables efficient generation of high-pressure ultrasound (highest S_{tx}), which is crucial for therapeutic UNS applications. Besides, using readily available PZT sheets in this context is well-established and will overcome complex microfabrication processes to fabricate cMUTs or pMUTs on a flexible substrate. pMUTs and cMUTs are favorable for sensing/imaging applications considering the higher receive sensitivity and bandwidth than PZT and the lower Q. The PZT sheets used here are available in various thicknesses, are pre-poled, and have sputtered Nickel electrodes (piezo.com). It should be noted that PZT must not be heated past its Curie temperature to prevent losing the initial poling effect [34]. Operating PZT at a maximum of half the Curie temperature is considered good practice to ensure long-term stability.

B. Simulations

To investigate the theoretical capabilities of the US arrays and to study different beam profiles, US simulations were performed using k-Wave, a MATLAB toolbox [35]. The model consisted of US sources generating waves with unitary pressure propagating through a medium modeled with the acoustic properties of soft tissue. The US sources were placed in an array, matching the dimensions of the fabricated US transducers. The computational grid points were spaced 50 μm apart, and a perfect matching layer surrounded the entire grid to prevent reflections at the grid's boundaries. The simulation ran for as long as it took the US wave to propagate to the end of the grid. The output consisted of root-mean-square (RMS) pressure maps.

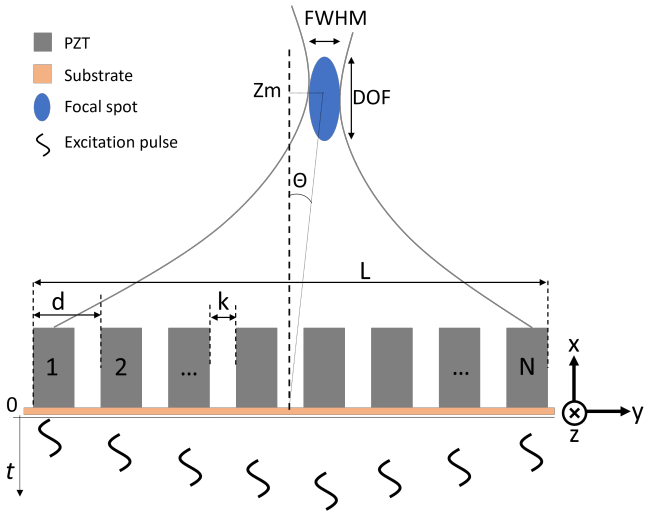

Fig. 3: Schematic representation of a US transducer array with important design dimensions and focal spot parameters. The excitations pulsed are plotted on a time axis (t), indicating the different phase delays to steer and focus the ultrasound beam. d: pitch, k: kerf, L: aperture, N: number of elements per row, Zm: focus distance, DOF: depth of focus, FWHM: full width at half maximum, θ: steering angle.

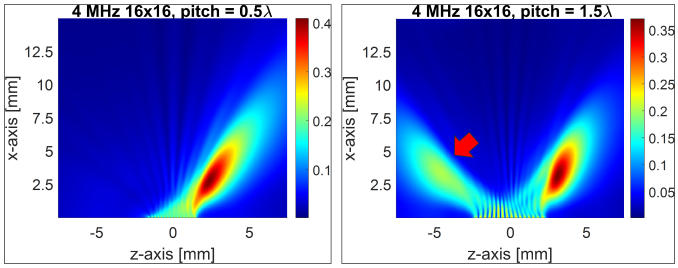

Fig. 4: Simulated ultrasound root-mean-square pressure profiles from a pitch-matched array (left) and an ill-designed transducer array (right). Unwanted grating lobes (indicated by the red arrow) appeared in the ill-designed transducer due to the array pitch larger than 0.5λ. Steering angle (Θ) = 35°, focus depth (Z_m) = 5 mm. The array exists on the zy-plane, perpendicular to the displayed simulation plane.

C. Device design

1) Design Considerations: The passive front end of the system consists of two arrays: an array of square activation

electrodes (AEs) to individually drive each PZT element of the array and an array of square contact pads (CPs) to connect to the back end. These two arrays are interconnected by interconnecting traces (ITs), connecting one AE to one CP. All ITs, AEs, and CPs are fabricated on a single level. The PZT elements share one common ground plane. In UNS, neural tissue is stimulated by where the US beam has the highest pressure, a region called the focal spot (FS). To precisely stimulate specific regions within neural tissue, it is essential to accurately steer the FS to the desired target. The transmitter array's design significantly impacts its performance, where the driving frequency (f), inter-element pitch (d), and the array's aperture (L, the total length of the transducer array) are the most critical design parameters. The measures discussed in this section are schematically depicted in Fig. 3.

First, the sound field of a transducer is divided into the near field (NF) and the far field. The NF is the region close to the transducer where the acoustic pressure goes through a series of amplitude variations. After the final on-axis maximum (representing the natural focus point), the beam diverges into the far field, and the pressure will gradually drop to zero. The NF distance depends on the transducer's frequency, L, and sound velocity in the medium (C, $\approx 1540m/s$ for soft tissue), following (2) [36].

$$NF = \frac{fL^2}{2.9C} \tag{2}$$

Within the NF region, the focal spot can be optimized and steered to different targets by adjusting the delay of the excitation pulses for each element in a phased array. To reach stimulation targets located deeper in the brain, the transducer must be designed so the NF extends far enough to include all stimulation targets. Another design parameter that must be considered is d, depicting the distance between elements in the array. For adequate beam forming, d must follow (3) to avoid grating lobes [37]. Grating lobes are unwanted maxima due to undersampling when d is too big for the desired steering angle θ. Respecting (3), d should be $\lambda/2$ to allow for a maximum steering angle ($\theta = \pm 90\,\mathrm{deg}$) without grating lobes. The importance of designing an array with appropriate d is illustrated with the simulation Fig 4. Here, beam steering with an ill-designed transducer results in an additional region with high pressure. In UNS, this can lead to side effects when unintended regions of the brain are stimulated.

$$d = \frac{\lambda}{1 + sin(\theta_{max})} \tag{3}$$

Two measures to evaluate the FS obtained by beam forming are the full width at half maximum (FWHM) and the depth of focus (DOF). The first is a measure for lateral resolution, and the second for axial resolution; both are proportional to the focus distance (Z_m), L, and λ trough (4) and (5) [22].

$$FWHM \propto \frac{\lambda Z_m}{L} \tag{4}$$

$$DOF \propto \frac{\lambda Z_m^2}{L^2} \tag{5}$$

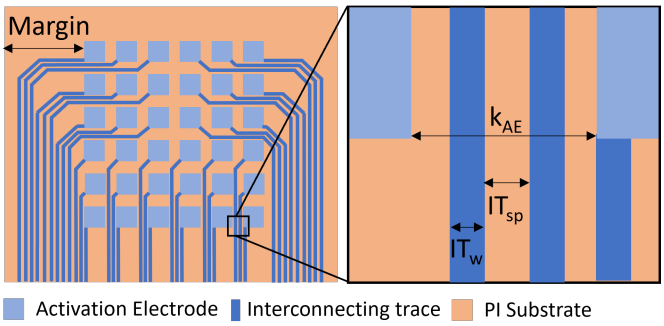

Fig. 5: Schematic representation of activation electrode array in a single-level design. The spacing between electrode pads (k_{AE}) limits the amount of interconnecting traces (ITs) that can pass in between, considering both the IT's width (IT_w) and the spacing (IT_{sp}). At higher frequencies, k_{AE} will decrease as the electrodes come closer together, leaving less space for ITs. The width indicated by *Margin* can also be a limiting factor since ITs from the upper half must pass next to the array on the polyimide (PI) substrate.

According to (2), (4), and (5), increasing f and L is beneficial since this improves spatial resolution (i.e., smaller FS) for more precise UNS and increases the NF to reach deeper targets. f and L can't be increased without limitation, however, for the following reasons:

- The array must fit on the substrate. In other words, L can't exceed the width of the substrate. The substrate width used here is 10 mm, taking the size of the rat skull into consideration.
- In a phased array, all elements must be addressed individually by interconnecting traces. In a single-level design, this means that an IT must pass in between electrode pads on the outside of the array to reach the ones in the middle, as shown in Fig. 5. Since increasing the frequency leads to a finer pitch through (3), the spacing between AEs (activation electrode kerf or k_{AE}) becomes smaller. This limits the number of ITs passing between the AEs, subsequently limiting N.
- Whereas the ITs from the upper half of AEs can travel straight down to the CPs, the traces from the upper half must pass to the side of the array (Fig. 5). When an array's area takes up most of the substrate, this leaves little room for ITs, which can limit the total amount of traces.
- The future back-end of the system (Vantage 256, Verasonics) can drive a maximum of 256 elements, limiting N to 16.

By fixing the dimensions for the ITs, AEs, and substrate width, a balance between L, f, and N is found. For relatively low ($< 1MHz$) frequencies, the factor limiting N is the array's aperture (L) that needs to fit on the substrate. Since d is large at low frequencies, an array with few elements will already lead to a large L. The fine d required at high frequencies will substantially limit the maximum number of ITs, limiting N. This trade-off is studied and visualized in Fig. 6. The dimensions for the ITs used here (Width = 5 μm,

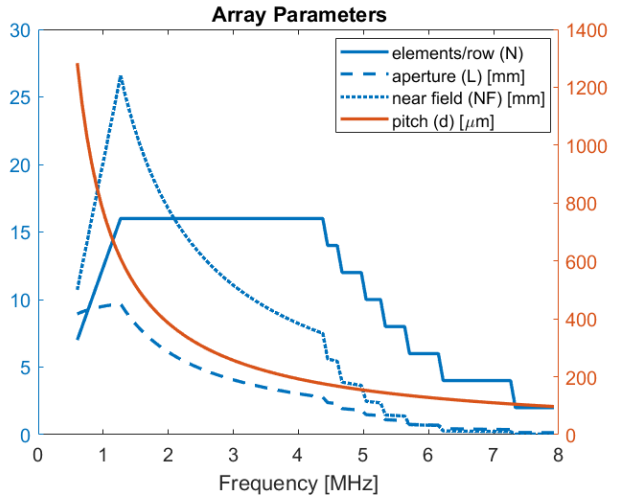

Fig. 6: Relationship between frequency and an array's maximum number of elements per row/column (N), aperture (L [mm]), near field distance (NF [mm]) and pitch (d [mm]). N is limited to 16 since the back end of the system can drive a maximum of 256 elements. The driving frequency is plotted on the x-axis, the blue lines corresponding to N, L, and NF are plotted on the blue y-axis on the left, and the orange line corresponding to the pitch is plotted on the orange y-axis on the right. Dimensions used here: IT width = 5 μm, IT spacing = 3.5 μm, Activation Electrode = 100x100 μm, substrate width = 10mm).

spacing = 3.5 μm) were considered the minimum dimensions viable. These were determined through the experimental fabrication of various test structures, as shown in Fig. A.2 and A.6, and by considering the capabilities of the lithography tools available to us (contact aligner with $3\mu m$ resolution and $\approx 1\mu m$ alignment accuracy in soft contact mode, MA/BA8, SUSS MicroTec).

2) Array layout: Considering the study from Fig. 6, it was concluded that the maximum f, for which the desired NF of 8 mm (to reach targets up to 8 mm deep) and maximum N of 16 is reached, was 4 MHz. Two 4 MHz arrays were designed: (1) a 16x16, 256-element array that was designed that the Verasonics Vantage back-end could drive and (2) an additional 30x30, 900-element array was designed to investigate the capabilities of the microfabrication approach presented here. The expected near field distance and the dimensions used for the different features in both arrays are listed in Table II. Both arrays are fabricated on a slightly wider PI substrate than the maximum width of 10 mm to ease the release process. The PI can be trimmed to 10 mm since all metal traces fell within this boundary.

The 16x16 array has a square array of AEs and a rectangular 8x32 array of CPs with ICs between both arrays. The dimensions of the ITs were optimized to the largest values possible while still being able to reach a 16x16 4 MHz array. The transition from an AE to an IC trace follows a tapered design to reduce stresses on the electrode-IC boundary. Once an IC trace leaves the AE arrays, it tapers into a wider 20 μm trace with 10 μm spacing leading to the CP. The CP array was designed to precisely match an 8x32 electrode array on a printed circuit board (PCB) developed in our group. This PCB could be flip-chip bonded to the CP array to act as an interface between the passive front-end and the back-end electronics. Three devices with a 16x16 AE array were produced, as depicted in Fig. 7: (1) a fully flexible device (Full-Flex), (2) a device that is fully flexible on the transmitter side but with a rigid silicon die remaining underneath the CPs (Rigid/Flex), and (3) a non-flexible reference sample where silicon supports the entire device. In the Rigid/Flex device, the silicon die underneath the CPs would support the bonding to a PCB. The metal electrodes fell within a region of 9.7 x 24.6 mm on a PI substrate measuring 13 x 28 mm.

Also, a 30x30 array was designed with minimum feature sizes considered viable. This array was intended to investigate the possibilities when approaching the limits of lithography techniques available to us. In this design, the CP array is identical to the transmitter array, making the design symmetrical. Only a fully flexible device with a 30x30 array was produced, no Rigid/Flex version. The metal electrodes fell within a region of 9.7 x 16.7 mm on a PI substrate measuring 12 x 18 mm.

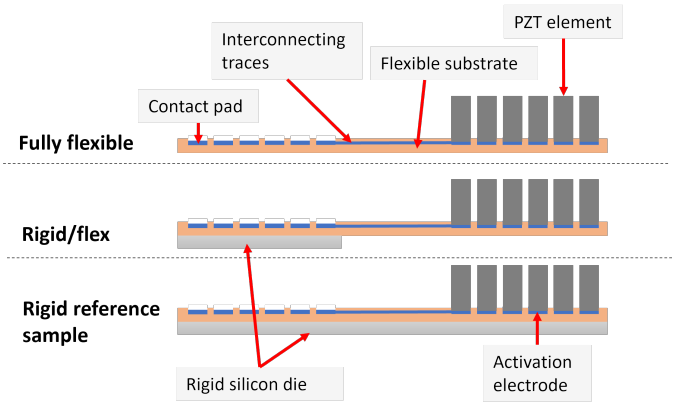

Fig. 7: Schematic representation of the devices that were designed with different degrees of flexibility.

Number of elements	16x16	30x30
IT width	8.6	5
IT spacing	4	3.5
Activation electrode	100x100	70x70
Contact pad	260x260	70x70
Aperture [mm]	2.9	5.7
Near field [mm]	8.3	29.4

TABLE II: Dimensions of two 4 MHz arrays. All values are μm unless stated otherwise. IT = interconnecting trace.

D. Device fabrication

1) On-wafer microfabrication method: The schematics in Fig. 8 show the different fabrication steps, and a detailed flowchart with all microfabrication processes is included at the end of the Appendix. 100 mm diameter, 300 μm thick, double-sided-polished silicon wafers were used as substrate.

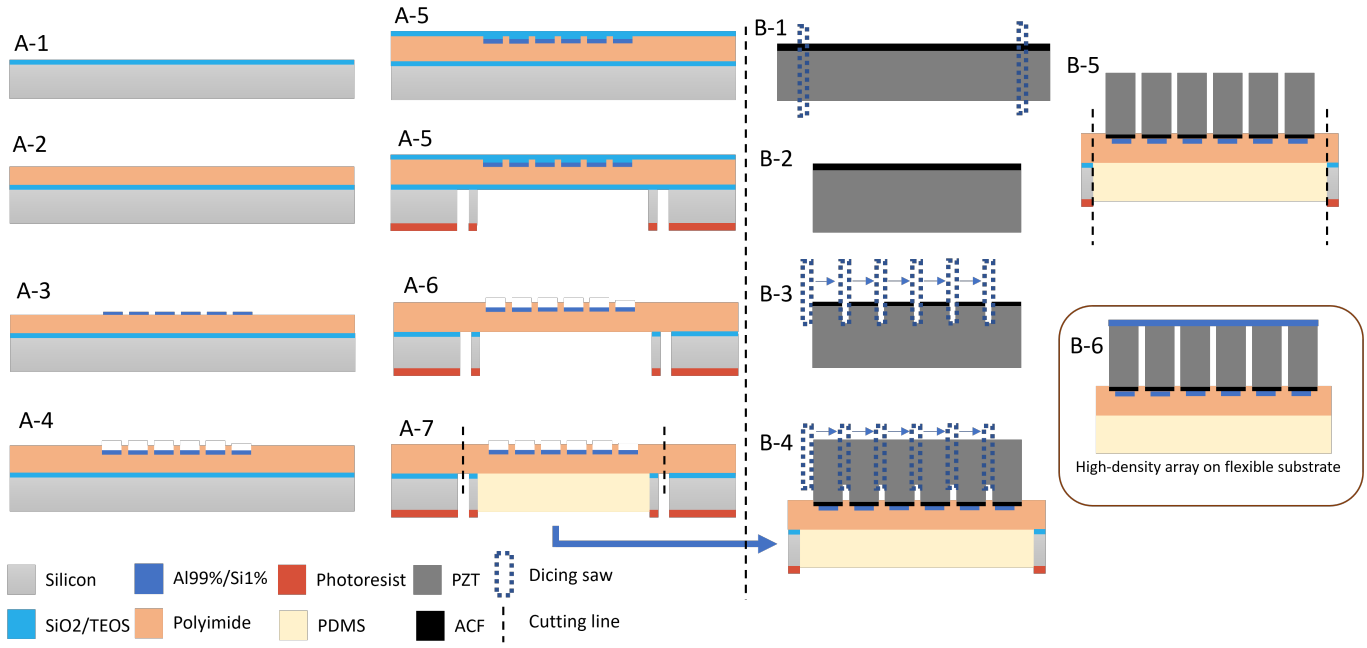

Fig. 8: Schematic representation of (A) the microfabrication steps and (B) the PZT integration process. A-1: 10 μm thick SiO_2 deposition on a 300 μm thick, double-sided-polished silicon wafer. A-2: Spin-coating and curing the PI base layer with 10 μm final thickness. A-3: Sputtering and patterning of 500 nm Aluminium 99% and Silicon 1% layer. A-4: 200 nm thick TEOS deposition. A-5: Deep reactive ion etching of the silicon from the backside using a thick photoresist mask. A-6: Wet etching of SiO_2 and TEOS. A-7: PDMS injection and release from the wafer. B-1 and B-2: Attaching the ACF and PZT-sheet dicing. B-3: pre-dicing by 30% of PZT thickness. B-4: Final dicing by 80% of thickness after attaching the PZT to the substrate. B-5: Release of the silicon frame. B-6: Attaching the common ground plant.

A 10 μm thick silicon dioxide (SiO_2) was deposited on the front of the wafer using PECVD at 400 °C (Concept 1, Novellus) (Fig. 8A-1). This layer will be used as a landing layer for deep reactive ion etching (DRIE) of silicon from the backside later in the process. A 19 μm PI base layer (Durimide 7520, Fujifilm) was spin-coated on the SiO_2 layer (Fig. 8A-2). Before coating, a dehydration bake at 150 °C for 2 minutes was performed on a hotplate to ensure good adhesion of the PI. This layer was cured in a low-pressure nitrogen environment. The temperature in the oven (CLH series, Koyo Thermo Systems) was ramped up for two hours to 350 °C, held at 350 °C for two hours, and then ramped back down for two hours to room temperature. The PI film shrank during curing to a 10 μm film. This thickness was measured using an optical reflectometer (FR-Scanner, ThetaMetrisis). The PI film was treated with short oxygen plasma (1 min, 600W, Tepla 300) to improve the adhesion of the metal thin film deposited next. A 500 nm Aluminium 99%Silicon 1% layer was deposited using a cryo-pumped magnetron sputtering system (Sigma 204, Trikon) at low temperature and power (25 °C, 1 kW). The metal was coated with 1.4 μm positive-acting photoresist layer (SPR3012, Megaposit) and soft-baked at 95 °C for 90 seconds (EVG 120, EVG). This photoresist was exposed using a contact aligner (120 mJ/cm^2 broadband, MA/BA8, SUSS MicroTec), followed by a post-exposure bake at 115 °C for 90 seconds and single-puddle development (MF-322, Megaposit) to produce a photoresist masking layer. Then, the aluminum was etched using reactive ion etching (Omega 201, Trikon) at 25 °C in a plasma containing Cl (30 sscm) and HBr (40 sscm) to create the AE array, CP array, and ITs (Fig. 8A-3). Afterward, the photoresist is removed using a short oxygen plasma (1 min, 600W, Tepla 300), acetone, and isopropanol (IPA) rinse. Standard oxygen plasma ashing of the photoresist is incompatible with the PI layer underneath since a high-power oxygen plasma will etch the PI.

The process continued with spin-coating a second, 4 μm thick PI layer (LTC9305, Fujifilm) to act as an insulation layer. This photosensitive, negative-acting PI can be patterned directly using standard lithography processing steps. After a soft-bake at 100 °C for 120 seconds, the PI film was exposed using the contact aligner (400 mJ/cm^2 I-line). The post-exposure bake was done at 50 °C for 60 seconds. Development was a multi-step process: the wafer was submerged in HTR-D2 (Fujifilm) for 90 seconds, rinsed with RER-600 (Fujifilm), submerged in RER-600 for 90 seconds, and rinsed with deionized (DI) water (Fig. 8A-4). Curing was performed following the same recipe as for the first PI layer. A descum treatment with oxygen plasma (1 min, 600W, Tepla 300) was performed to remove any small PI particles left behind during development. The final film thickness was $\approx$2.5 μm, measured using a stylus profilometer (Dektak 8). Then, a 200 nm tetraethylorthosilicate (TEOS) layer was deposited using PECVD on the front side at 300 °C (Fig. 8A-5). Processing at this temperature is still within the thermal budget of PI, which is one of the benefits of using this polymer. The TEOS layer makes the layer stack compatible with the DRIE machine (Rapier Omega i2L, SPTS

Technologies) and protects the PI layer during silicon etching from the back since the etch rate of TEOS is low.

Due to the strong adhesion between PI and the silicon/SiO_2 substrate, through-wafer DRIE was performed from the backside, landing on the previously deposited SiO_2 landing layer (Fig. 8A-6). By selectively removing the 300 μm silicon underneath the parts containing the arrays and ITs, the devices could simply be cut out from the wafer. A small silicon frame was left behind to provide support during the integration of the PZT transducer elements. Backside processing started with coating a thick positive photoresist (AZ12XT-20PL) to mask silicon DRIE. This photoresist was coated after a hexamethyldisilazane (HMDS) treatment, soft-baked at 110 °C for 3 min, and exposed using the mask aligner (110 mJ/cm^2, I-line). After a post-exposure bake at 90 °C for 60 seconds, the photoresist was developed in two 60-second puddles (MF-322, Megaposit) and hard baked at 115 °C for 3 minutes. DRIE was performed at 20 °C in a plasma containing SF_6. The process was monitored using the stylus profilometer to measure the depth of the cavity. The SiO_2 and TEOS layers were removed by wet etching using BHF 1:7. Finally, PDMS (Sylgard 184, Dow Corning) was injected into the cavities made by DRIE on the backside (Fig. 8A-7). The cavities were filled completely, and any excess PDMS was removed using a blade, planarizing the surface simultaneously. The PDMS was partially cured on a hotplate for 10 mins at 125 °C. The purpose of this PDMS was to provide support during PZT integration and to prevent PI from curling once it is released from the wafer. The partially cured PDMS was stiff enough for the device to be cut out of the wafer. The PDMS was only partially cured to provide proper bonding with the PDMS encapsulation at the final stage of device assembly.

2) Ultrasound transducer integration: The fabrication process to integrate PZT elements on top of the AEs starts with a commercially available PZT sheet (510 μm thick, pre-poled PZT5A, T120-A4NO-2929, piezo.com). The theoretical resonance frequency through calculation according to (1) of this PZT sheet was 4.4 MHz, most closely matching the desired frequency of 4 MHZ of the options that were available. A schematic overview of the process is provided in Fig. 8B. The PZT sheet is cut into smaller dies using a dicing saw with a 50 μm thick blade (DAD 3240, DISCO) (Fig. 8B-1). The blade thickness will determine the kerf ((K), i.e., the spacing between elements, see Fig. 3) in the subsequent fabrication steps. A small kerf is, therefore, beneficiary, as this will increase the total active area in the transmitter array. However, decreasing the kerf will increase the minimum bending radius, as the top of the PZT elements touching each other will prevent bending the array any further. This concept is explained in more detail in Appendix I-A. The arrays designed here have a theoretically calculated minimum bending radius of 2.2 mm.

A spindle speed of 30.000 rpm was used for all cuts in the process. These initial dies were slightly bigger than the transmit array dimensions. Anisotropic electrically conductive pressure-sensitive adhesive transfer film ((ACF), 25 μm thick, ARclad 9032-70, Adhesives Research) is cut into the die size and applied using a hand roller. Then, the die was diced into a chip matching the size of the transmit array (Fig. 8B-2). Dicing the PZT and the ACF into the correct size simultaneously ensured the chip had sharp edges, which is essential for blade alignment in the following steps. The chip is pre-diced from the side containing the ACF by 30% of its thickness (feed speed: 2 mm/s) (Fig. 8B-3). Afterward, the chip is aligned with the pre-diced side of the chip to the AE array under optical microscope vision. The minimum pad size used in this study was 70 μm, which was slightly bigger than in the process demonstrated by Costa et al., where 50 μm pads were viable because of the higher performance ACF that was used. The chip is bonded to the array by applying pressure for one minute, using a hand roller while heating the substrate to 60 °C on a hotplate. Once the chip was adequately bonded to the array, it was diced on the opposite side from the pre-dicing by 80% of the total thickness to create free-standing PZT elements (feed speed: 0.3 mm/s). At this point, the device could be released from the silicon frame by cutting it out (Fig. 8B-5). Finally, a 25 μm thick aluminum film was attached using silver conductive adhesive paste (42469, Alfa Aesar) on top of all elements to create the common ground plane (Fig. 8B-6).

3) Encapsulation: Before the device was encapsulated, two wires (Tungsten 99.95%, 0.05mm ∅, annealed) were attached to drive the transducer using silver paste. One wire was attached to the common ground plane, and the other to the CPs. Because the transducer produces planar waves in this current study, all contact pads are shorted using the silver paste to drive all PZT elements simultaneously. Afterward, the device was wholly encapsulated in PDMS to (1) protect the transducer array, CPs, and interconnecting wires and (2) serve as a biocompatible barrier between biological tissue and the PZT elements. Encapsulation in the same material as the substrate was impossible since PI needs to be cured above 300 °C, temperatures that will negatively impact the PZT element's performance. The encapsulation was performed using an open mold design. The mold (Fig. A.3) was designed using CAD software (Solidworks 2022) and 3D printed with a high-resolution resin printer (Max X, Asiga) and high-performance resin (Tech Clear, Moiin). After placing the device inside, PDMS was poured into the mold and planarized using a blade. It was cured on a hotplate at 125 °C for 20 minutes. This resulted in a final thickness of 1.4 mm.

E. Ultrasound characterization set-up

As a proof of concept, it was tested whether the fabricated devices could produce a US planar wave and characterized the beam profile. These measurements will provide essential insight into whether the design and fabrication method presented here is viable. To perform the measurements, the flexible arrays were mounted on a glass slide for measurements in a flat state or in a 3D-printed holder (Max X, Asiga) to test the array in a curved state (Fig. 11D and A.4). The curvature of the holder has a radius of 8.8 mm, matching the model of a rat's brain [38]. For comparing the results, three reference samples were produced: a non-flexible 4 MHz 16x16 array on a silicon die (Fig. A.10), a single 4 MHz PZT element the

size of the 16x16 array, and a similar element matching the 30x30 array.

To characterize a sample, it was connected to a function generator (DG 4202, RIGOL) and submerged in distilled water. A 3-axis positioning system (VK-62100, Gampt) was programmed to move a fiber-optic hydrophone (Fibre diameter 125 mm, Precision Acoustics, FOHSv2), scanning an indicated line or plane. A picture of the setup is shown in Fig. A.5. The hydrophone was moved in 200 μm steps. After each step, the function generator was triggered to drive the transducer with a 10V peak-to-peak sinusoidal burst consisting of 20 pulses, and the oscilloscope (DSO-X 3032A, Keysight) recorded the preamplified electric signal from the hydrophone. This measurement was triggered with a short delay after the acoustic signal was generated to prevent the pickup of electromagnetic interference. The positioning system, oscilloscope, and function generator were operated via custom MATLAB software. This enabled the measurement of beam profiles in different planes and to sweep US parameters, such as f. Each measurement consisted of 16000 voltage values averaged over 16 separate samples. These average voltages were converted to pressure observations using the frequency-dependent hydrophone sensitivity. From here, the maximum peak-to-peak pressure was calculated and plotted by subtracting the minimum from the maximum pressure.

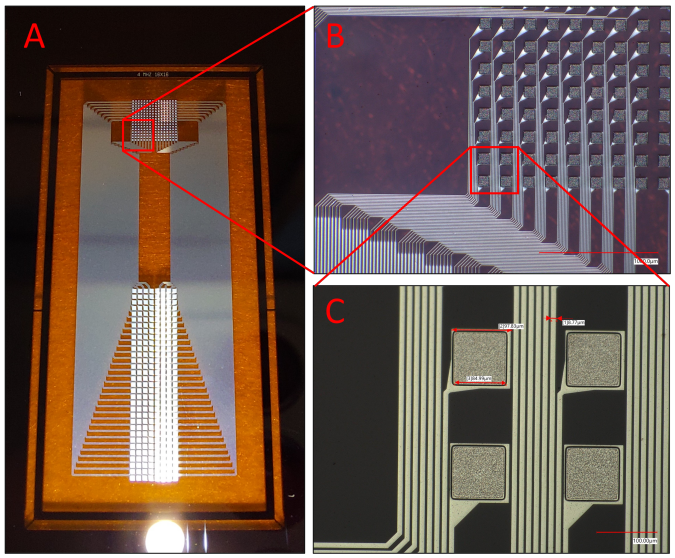

Fig. 9: A: Photograph of the finished device in-wafer showing the 16x16 activation electrodes on the top and the 8x32 contact pad array at the bottom. The orange transparent polyimide and silicon frame are clearly visible since through-wafer cavities are etched in the back by DRIE. B: Micrograph of the lower left quadrant of the array and the interconnect traces. C: Four activation electrodes with properly aligned openings in the polyimide.

III. Results

A. Electrode arrays on polyimide substrate

After the on-wafer microfabrication process, ready-to-release metal electrode arrays on a flexible polyimide substrate were obtained. Before the prototypes were released from the wafer, they were inspected with digital optical (Fig. 9A-C, Keyence VHX-7000) and laser-scanning microscopes (Fig. 9D, Keyence VK-X250). The 4 MHz 16x16 transmitter array comprises 256 square activation electrodes with a 100 μm edge length, distributed at 193 μm inter-electrode pitch, and the 30x30 array has 900 electrodes with a 70 μm edge length. By measuring devices processed in different wafers (Fig. 9C), it was concluded that the fabricated dimensions were within 2% of the design specifications. Fig. 9A shows the entire device with the 16x16 transmitter array, the 8x32 array of contact pads, and interconnect traces between the two arrays. Fig. 9B shows the ITs taper from 8.6 μm wide ITs close to the array into less fragile 20 μm wide traces. After curing the polyimide insulation layer on top of the Aluminium99%Silicon1%, the appearance of this metal visibly changed. By visual inspection, it was concluded all traces remained intact, however. This was confirmed by measuring the electrical resistance over eight 2 cm long, 500 nm thick metal traces with different widths (5-80μm). The expected values for these resistances were also calculated using the resistivity of Aluminium99%Silicon1% ($\rho = 2.60 * 10^{-8}\Omega/m$). By comparing the measured values to the expected values (Fig. 10B, we could conclude the metal traces perform as expected. Lastly, to check whether the insulation layer provided by the second layer of PI was properly developed, we measured the height profile from the PI's surface to the electrode (Fig. 10A). The opening to the electrode is 85 μm wide and has a step height of 1750 nm, which the 25 μm thick ACF could easily overcome.

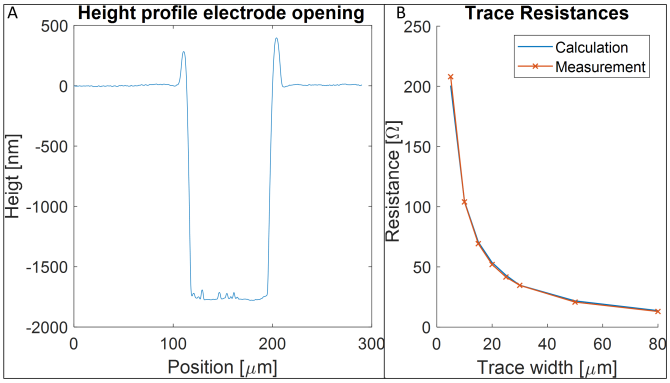

Fig. 10: A: height profile of an opening in the polyimide insulation layer above an activation electrode, obtained with a stylus profilometer (Dektak 8) in a 16x16 array. B: The measured and calculated electric resistances (y-axis) of 2 cm long, 500 nm thick Aluminium99%Silicon1% traces with varying widths (x-axis).

B. PZT integration and device encapsulation

Because cavities were etched in the silicon on the backside of the wafer, the devices could be cut out (Fig. A.7). This proved a simple method and overcame additional dicing steps to release the devices that would potentially cause damage. A tiny silicon frame was left in place to prevent the device from curling due to internal stresses in the PI (Fig. 11A).

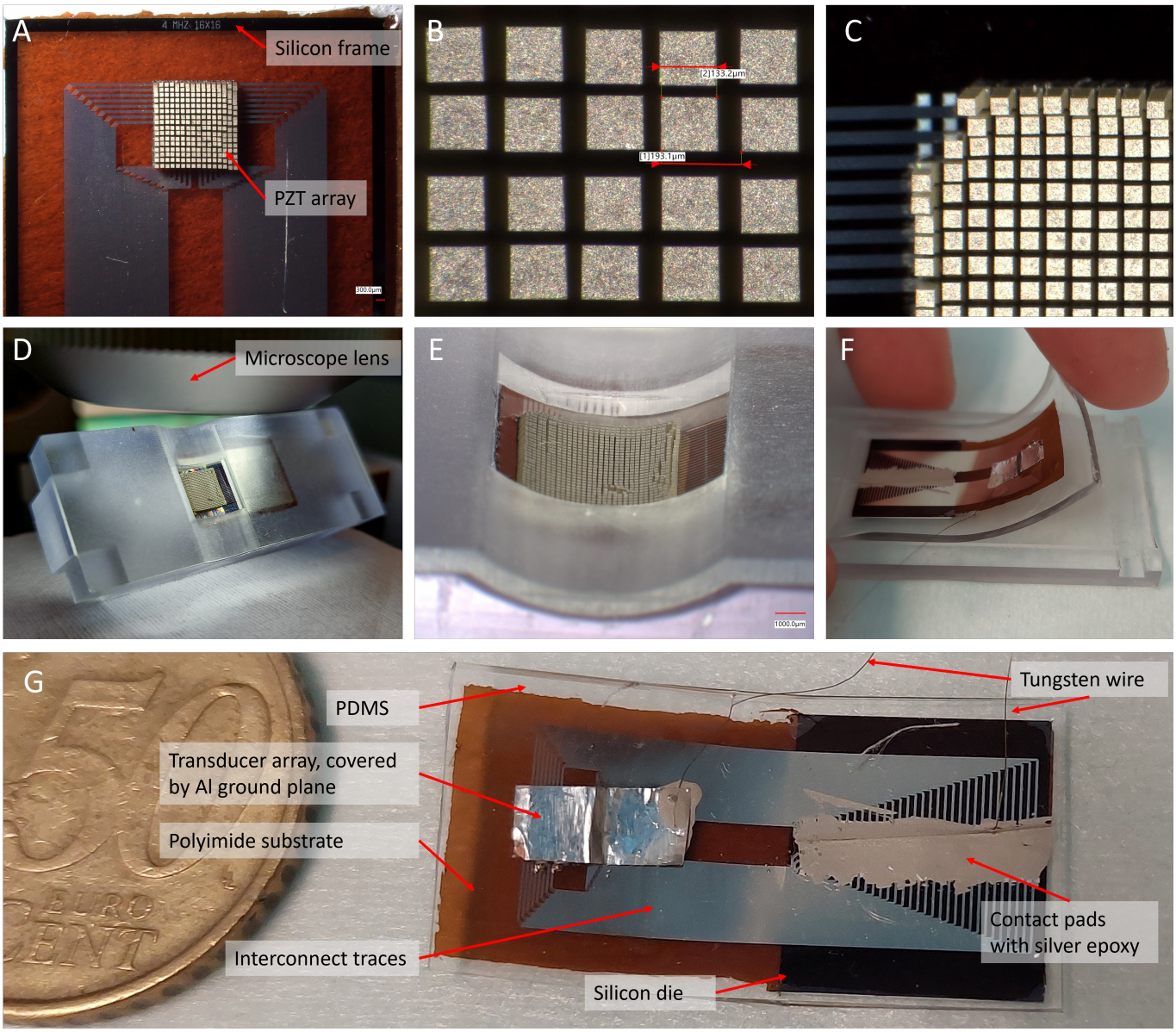

Fig. 11: Pictures of PZT integration and device assembly. A: PZT attached to the electrode array and diced into individual elements. The device is released from the wafer but still supported by a small silicon frame created during DRIE. B: Zoomed-in picture showing the PZT elements with a 133 μm edge length and 193 μm pitch. C: Five elements in the upper left corner came off during dicing. D: The 30x30 array in a curved state, clamped in the 3D printed holder underneath the microscope lens. E: view from the microscope lens in picture D, showing the array bent at an 8.8 mm radius. F: The Rigid/Flex device could be peeled from the 3D mold once the PDMS was cured. G: A fully assembled 16x16 Rigid/Flex device.

The PZT integration process started by pre-dicing a PZT and placing it on the AE array with ACF. Even though the bond seemed strong, the PZT came off during the final dicing step in early samples. The dicing process succeeded by reducing the feed speed from 1 mm/s to 0.3 mm/s. The dicing machine's fine stage control was used to align the blade's edge to the PZT die. This method resulted in the proper alignment of the pre-dicing cuts to the final cuts. The bonding strength of the ACF was enough to keep the PZT elements adhered to the electrode during the dicing, although some elements were tilted, especially in the outermost ring. A 16x16 array of individual PZT elements at 193 μm pitch and 60 μm kerf was fabricated, with all elements remaining after the final dicing (Fig. 11A,B) and thus 100% yield. In another sample, five elements in the corner of the array came off during dicing (Fig. 11C), resulting in 98% yield. The 30x30 array was also produced successfully with a 98% yield. Six elements were lost in the outer ring, and one element was lost in the middle of the array. The silicon frame around the device was removed after attaching the tungsten wires and ground plane. The removal of the frame led to slight substrate curling, which was overcome by gluing the sample in the mold with a first layer of PDMS. After the device was encapsulated entirely in PDMS, flexibility was maintained while reducing the overall

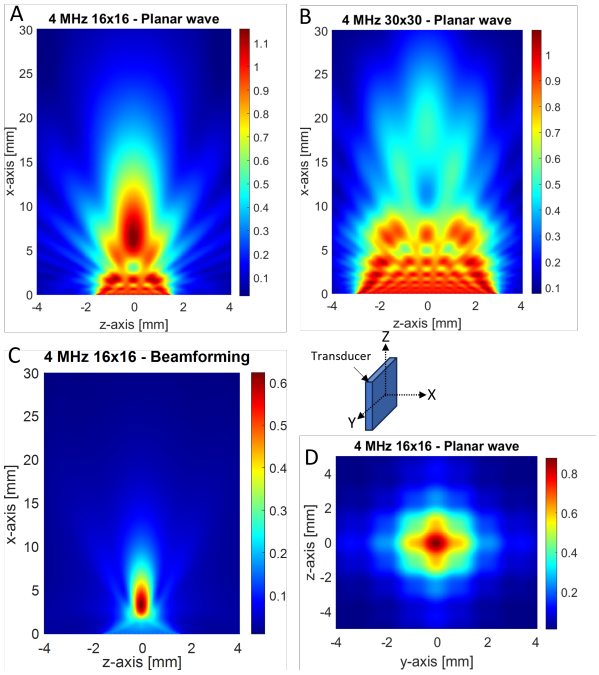

Fig. 12: Simulated pressure profiles, depicted as unitary root-mean-square pressure maps. The coordinate system relative to the transducer is schematically shown. A and B: Planar waves produced by the 16x16 and 30x30 array. C: The 16x16 was driven as a phased array, focusing the beam at Z_m = 5 mm. D: A cross-section of the focal spot parallel to and 6 mm from the transducer.

tensile stress of the device (11F). A fully assembled and capsulated device is shown in Fig. 11F, measuring This version is flexible at the transmitter array but rigid at the contact pads. The fully flexible version and the version with the 30x30 array are depicted in Fig. A.8.

C. Ultrasound characterization

1) Simulations: The potential beam profiles of the devices were simulated in k-Wave. These beam profiles served as a reference to compare with the measured US beam profiles. Fig. 12A and B show the simulated planar waves produced by the 16x16 and 30x30 arrays. As a proof of concept study, all devices were driven to produce planar waves, and the US beam pressure profiles were recorded. First, the US beam profile for a planar wave produced by the 16x16 4 MHz array was simulated to compare this profile to the measurements (Fig. 12A). The 30x30 transducer produces a larger beam profile with an area of high pressure close to the transducer but with a less clearly defined natural focal spot (Fig. 12B). Since the transducer's design was optimized beam steering, driving it as a phased array would significantly improve its performance since it enables electronic focusing -resulting in a significantly smaller focal spot (Fig. 12C). The 16x16 transducer produces a clear natural focus spot around x = 6 mm, depicted in the cross-section plane parallel to the transducer 6 mm from the transducer's face (Fig. 12D).

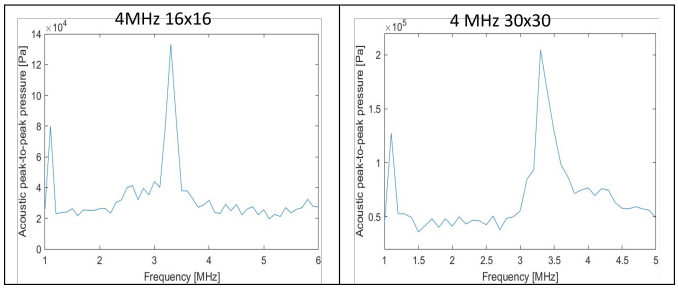

Fig. 13: The driving frequency was swept to find the resonance frequency. The resonance frequency was found to be 3.3 MHz for both devices.

2) Measurements: For the US characterization measurements, the resonance frequency was determined for each device and set as the working frequency for the subsequent measurements. It was obtained by sweeping the frequency with 0.1 MHz increments while recording the output peak-to-peak pressure of the transducer with the hydrophone, as shown in Fig. 13. The highest pressure was recorded at 3.3 MHz for both the 16x16 and 30x30 arrays, which was lower than expected since the array was designed to operate at 4 MHz. As a reference, the resonance frequencies of PZT elements with the size of the 16x16 array and the size of the 30x30 array were obtained, which were 4.6 MHz for both elements. At 3.3 MHz, the near field of the array extends to 6.6 mm through the calculation following (2). Next, cross-sections of the US beam profiles were obtained for all devices measured in a plane parallel to the transducer. This measurement plane was located 6 mm from the transducer, just within the near field (Fig. 14). All devices could generate ultrasound waves, indicating successful design and fabrication. The 16x16 arrays have a peak pressure output of 130-140 kPa, whereas the 30x30 has a higher peak of ≈450 kPa. The Rigid/Flex 16x16 device produces two separate focal spots, around 1 ∅ mm. The fully flexible device (Fig. 14B) does not have a clear focal spot but a region of high pressure about the same size as the transducer of 3 ∅ mm. Considering the FWHM region of the 30x30 array, an area of around 4 ∅ mm can be identified (Fig. 14C). This is comparable to the simulation. A peak pressure region of approximately 1.5 ∅ mm can be seen within this region. Two additional measurements are shown for the 16x16 Rigid/Flex device (Fig. 14A). It was tested in a curved state, clamped in the designated holder, conforming to an 8.8 mm radius (Fig. 14A). The peak pressure remained similar to the flat state, but one of the two focal spots became more apparent. Additionally, a measurement along the X-axis was obtained. This ZX plane is parallel to the US propagation direction and perpendicular to the transducers. It starts at a 0.5 mm distance from the array and extends up to 10 mm. It seems there are two US beams, with a region of low pressure separating them. The highest pressure is seen close to the transducer, decreasing from x = 2 mm onwards. Finally, to investigate the flexible substrate's influence on the array's performance, the US generated by the rigid reference array was recorded (Fig. A.10). It gave a relatively well-defined focal spot with a ≈1 mm diameter

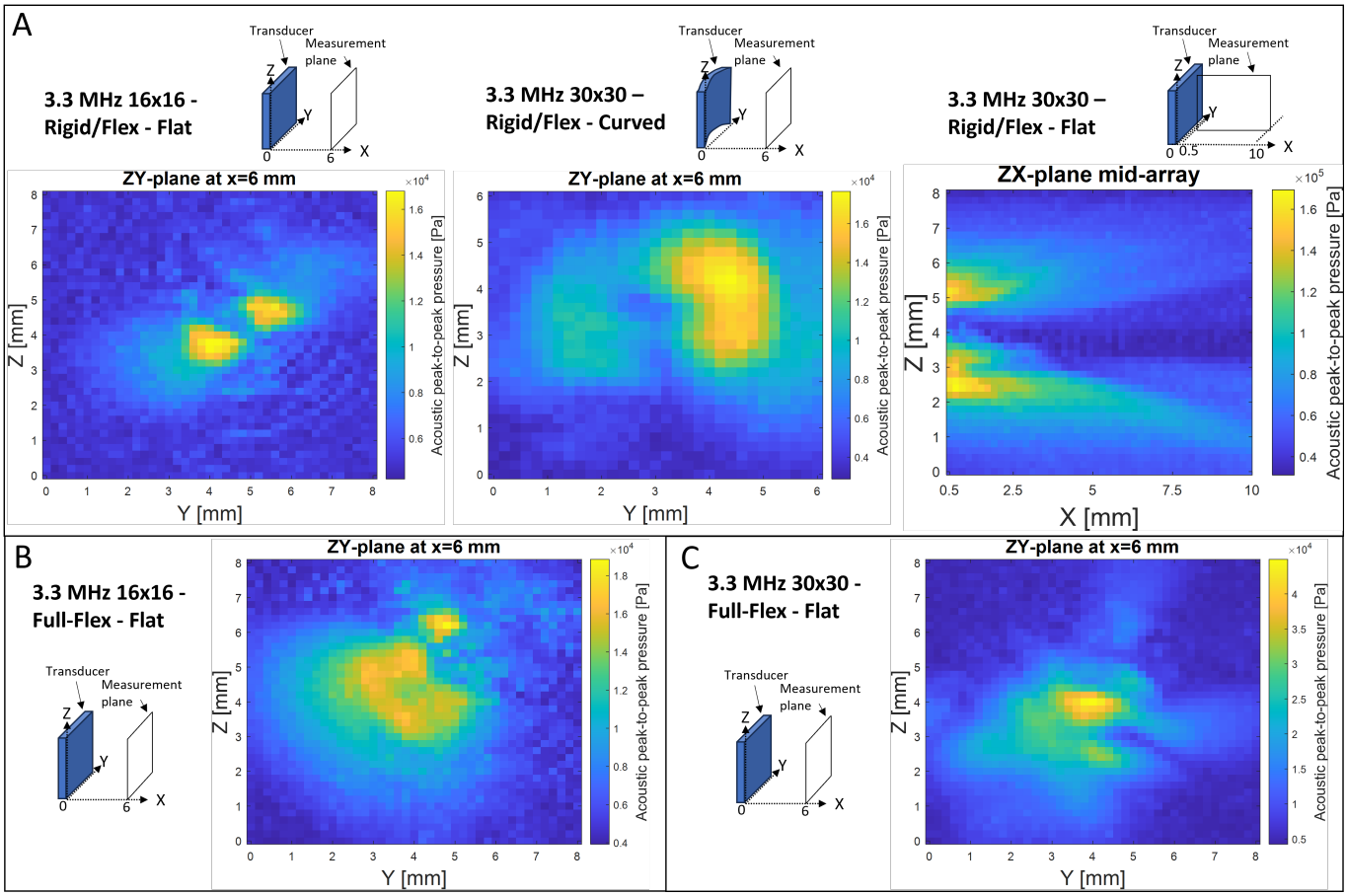

Fig. 14: Measured ultrasound beam profiles. The measurement plane related to the transducer is depicted in the diagram to the left of each plot. The arrays were driven at the measured resonance frequency of 3.3 MHz. A: The 16x16 Rigid/Flex device in both flat and curved state at 8.8 mm radius. B: the fully flexible version of the same device in a flat state. C: The fully flexible 30x30 device in a flat state.

-comparable to the simulation- and a peak pressure of 290 kPa.

IV. Discussion

Here, working prototypes for a novel flexible ultrasound neurostimulator were presented. The main innovation of this study is a 4 MHz pitch-matched transducer array on a flexible substrate. The combination of these two features is unique. The array's design is optimized for electronic beam steering without grating lobes. The relationship between the driving frequency and the achievable number of elements in the array in a single-level design was studied. It was concluded that 4 MHz was the optimal driving frequency and created three devices featuring arrays at this frequency: a fully flexible device with a 4 MHz 16x16 transmitter array, a device with an identical transmitter but a rigid contact pad array, and a fully flexible device with a 4 MHz 30x30 array. These devices were produced using a newly developed microfabrication process and optimized PZT-integration technique.

Once the microfabrication process was optimized, reproducible results were acquired. Some difficulties that were overcome in the process are depicted in Fig. A.9. Multiple wafers could be processed per batch with a total processing time of about three days. The thermally stable polyimide substrate enabled high-temperature processes such as PECVD at 300°C. A downside of polyimide is the time-consuming (around 6 hours) curing step required, which limits the throughput rate. In the current process, we used a 10 μm SiO_2 landing layer for DRIE. However, it proved challenging to remove this silicon dioxide by wet etching. The SiO_2 thickness was chosen to provide mechanical support to the large PI membranes during the DRIE steep. However, since the PI alone proved strong enough to span the cavity once the SiO_2 was removed, a thinner SiO_2 layer is advised for future versions since this will ease the removal by wet etching.

As a proof of concept study, the most important finding of the US characterization experiments is that all devices could produce US waves. This proves that the design and fabrication approach did not contain crucial flaws that would result in defective devices. Planar waves with peak pressure outputs of approximately 140 kPa for the 16x16 array and 450 kPa for the 30x30 array were achieved. In future work, these pressures could be increased by electronically focusing the ultrasonic waves generated by the individual elements. Simulations showed the potential capabilities of the transmitter being driven as a phased array, resulting in a smaller focal spot

steered at an angle. Another observation from the simulation is the shift in the near-field distance (NF). This is a common phenomenon in arrays with small Fresnel numbers [39]. For the 4 MHz 16x16 array, this led to a discrepancy between the calculated NF at 8.1 mm and the simulated value of 6 mm. Moreover, the measured resonance frequency of 3.3 MHz was lower than expected, resulting in a further decrease of NF and a larger focal spot. We found that f_r decreased once the PZT was diced from a sheet (length>>thickness, f_r = 4.6 MHz) into high-aspect-ratio individual elements (length<thickness, f_r = 3.3 MHz). This change in geometry probably led to a shift in vibration mode, changing from thickness vibration mode to bar extension mode. In bar extension mode, resonance frequencies tend to decrease, whereas the electromechanical coupling factor can increase [40]. Future studies could investigate using PZT sheets with custom-made thickness to achieve an array at the correct 4 MHz f_r. Moreover, using different PZT materials with higher coupling factors, such as PZT5H and PMN-PT, could significantly improve the pressure output. However, the aforementioned materials are not superior for all applications because they are more expensive, fragile, and have a smaller thermal budget. Other ways to improve the pressure output worthy of future research include (1) employing matching and backing layers, (2) driving the PZT at a higher voltage, (3) using a different encapsulation, and (4) optimizing the US beam profile. The current PDMS encapsulation could have suffered from non-uniformity, which can cause dispersion of the US beam. As an alternative, Paralyne-C could be considered. This is a frequently used encapsulation that can be deposited as a highly uniform film with micrometer-scale thickness. It was not used here since it was expected to provide too little structural support, leaving the array fragile. Or, by using a different material with the right acoustic properties, the encapsulation could simultaneously act as a matching layer between the PZT and soft tissue.

Through the US characterization measurements, it was found that the focal spots produced by our devices were larger and less clearly defined than in the simulated case. The simulation assumes a perfectly flat array where all elements are identical and functional. This was not the case in the actual devices, as some elements were lost, and others were tilted. During dicing, the elements on the outer ring of the array were especially problematic. This might be because these elements are most forcefully sprayed with cooling water while dicing. If the design allows, the array can be designed with an extra outer ring of dummy PZT elements to protect the functional elements. Additionally, using an ACF with stronger adhesion and applying the PZT with more uniform pressure could help overcome this problem. It could have been the case that some elements were inadequately bonded to the electrode or ground plane. Moreover, in the current setup, it was impossible to identify individual non-functioning elements. A probable cause of the split beam in Fig. 14A is a region of dead pixels/non-functioning elements in the middle of the array where low pressure was measured. To improve, besides optimizing the ground plane (e.g., sputtering a metal film on top), one of the characteristics of phased arrays could be used. Since in phased arrays, all elements can be driven individually, one could characterize the array by driving and measuring the elements one by one. Then, faulty elements could be accounted for by adjusting the phasing of the other elements. Moreover, the phasing could be adapted for curvature by equipping the array with curvature sensors. Future studies are required to optimize the current devices and to interface them with the Verasonics US driver back end. Then, the next step is to test the devices on biological samples and in animal studies.

V. Conclusion

In this study, an innovative microfabrication process that unites a flexible substrate with a pitch-matched 4 MHz PZT array was introduced - an unprecedented combination. Each prototype has demonstrated the capability to generate planar ultrasonic waves, prepared to be integrated as phased arrays for electronic beam steering. As the field progresses, considering future optimizations, the potential uses of these devices expand into the realm of using ultrasound for neurostimulation in humans. This could become a way to treat different brain disorders in the future.

VI. Acknowledgements

I thank Dr. Tiago Costa for supervising my MSc thesis project. You have been a great and approachable mentor. I learned a lot and had a very enjoyable time in your research group. Thank you, Gandhi Wardhana, for sharing your endless knowledge about microfabrication. As we discussed, the lessons learned from the microfabrication process expand to life in general. I will keep your quote 'haste is waste' in mind during future work. Lastly, I would like to thank the staff of the Else Kooij Laboratory for teaching me how to use the tools inside the cleanroom.

References

[1] E. Fuchs and G. Flügge, "Adult neuroplasticity: More than 40 years of research," *Neural Plasticity*, vol. 2014, 2014.

[2] V. L. Feigin and G. . N. Collaborators, "Global, regional, and national burden of neurological disorders, 1990–2016: a systematic analysis for the global burden of disease study 2016," *The Lancet. Neurology*, vol. 18, p. 459, 5 2019.

[3] PAHO, "The burden of mental disorders," 2021.

[4] O. D. Howes, M. E. Thase, and T. Pillinger, "Treatment resistance in psychiatry: state of the art and new directions," *Molecular Psychiatry*, vol. 27, p. 58, 1 2022.

[5] Z. Warraich and J. A. Kleim, "Neural plasticity: the biological substrate for neurorehabilitation," *PM R : the journal of injury, function, and rehabilitation*, vol. 2, 2010.

[6] C. Stengel, C. Sanches, M. N. Toba, and A. Valero-Cabré, "Things you wanted to know (but might have been afraid to ask) about how and why to explore and modulate brain plasticity with non-invasive neurostimulation technologies," *Revue neurologique*, vol. 178, pp. 826–844, 10 2022.

[7] S. Carmer, "Harnessing neuroplasticity for clinical applications," *Brain*, vol. 134, pp. 1591–1609, 6 2011.

[8] T. M. Herrington, J. J. Cheng, and E. N. Eskandar, "Mechanisms of deep brain stimulation," *Journal of Neurophysiology*, vol. 115, pp. 19–38, 1 2016.

[9] D. C. Klooster, A. J. de Louw, A. P. Aldenkamp, R. M. Besseling, R. M. Mestrom, S. Carrette, S. Zinger, J. W. Bergmans, W. H. Mess, K. Vonck, E. Carrette, L. E. Breuer, A. Bernas, A. G. Tijhuis, and P. Boon, "Technical aspects of neurostimulation: Focus on equipment, electric field modeling, and stimulation protocols," *Neuroscience and biobehavioral reviews*, vol. 65, pp. 113–141, 6 2016.

[10] J. Blackmore, S. Shrivastava, J. Sallet, C. R. Butler, and R. O. Cleveland, "Ultrasound neuromodulation: A review of results, mechanisms and safety," *Ultrasound in Medicine and Biology*, vol. 45, pp. 1509–1536, 7 2019.

[11] G. Darmani, T. O. Bergmann, K. B. Pauly, C. F. Caskey, L. de Lecea, A. Fomenko, E. Fouragnan, W. Legon, K. R. Murphy, T. Nandi, M. A. Phipps, G. Pinton, H. Ramezanpour, J. Sallet, S. N. Yaakub, S. S. Yoo, and R. Chen, "Non-invasive transcranial ultrasound stimulation for neuromodulation," *Clinical Neurophysiology*, vol. 135, pp. 51–73, 3 2022.

[12] B. Feng, L. Chen, and S. J. Ilham, "A review on ultrasonic neuromodulation of the peripheral nervous system: Enhanced or suppressed activities?," *Applied Sciences 2019, Vol. 9, Page 1637*, vol. 9, p. 1637, 4 2019.

[13] D. P. Darrow, "Focused ultrasound for neuromodulation," *Neurotherapeutics 2018 16:1*, vol. 16, pp. 88–99, 11 2018.

[14] R. L. King, J. R. Brown, W. T. Newsome, and K. B. Pauly, "Effective parameters for ultrasound-induced in vivo neurostimulation," *Ultrasound in Medicine and Biology*, vol. 39, pp. 312–331, 2013.

[15] S. S. Yoo, A. Bystritsky, J. H. Lee, Y. Zhang, K. Fischer, B. K. Min, N. J. McDannold, A. Pascual-Leone, and F. A. Jolesz, "Focused ultrasound modulates region-specific brain activity," *NeuroImage*, vol. 56, pp. 1267–1275, 6 2011.

[16] W. Lee, P. Croce, R. W. Margolin, A. Cammalleri, K. Yoon, and S. S. Yoo, "Transcranial focused ultrasound stimulation of motor cortical areas in freely-moving awake rats," *BMC Neuroscience*, vol. 19, 9 2018.

[17] S. S. Yoo, K. Yoon, P. Croce, A. Cammalleri, R. W. Margolin, and W. Lee, "Focused ultrasound brain stimulation to anesthetized rats induces long-term changes in somatosensory evoked potentials," *International Journal of Imaging Systems and Technology*, vol. 28, pp. 106–112, 6 2018.

[18] H. Kim, S. Kim, N. S. Sim, C. Pasquinelli, A. Thielscher, J. H. Lee, and H. J. Lee, "Miniature ultrasound ring array transducers for transcranial ultrasound neuromodulation of freely-moving small animals," *Brain Stimulation*, vol. 12, pp. 251–255, 3 2019.

[19] R. Beisteiner, E. Matt, C. Fan, H. Baldysiak, M. Schönfeld, T. P. Novak, A. Amini, T. Aslan, R. Reinecke, J. Lehrner, A. Weber, U. Reime, C. Goldenstedt, E. Marlinghaus, M. Hallett, and H. Lohse-Busch, "Transcranial pulse stimulation with ultrasound in alzheimer's disease—a new navigated focal brain therapy," *Advanced Science*, vol. 7, p. 1902583, 2 2020.

[20] G. Paxinos and C. Watson, *The Rat Brain in Stereotaxic Coordinates*. Elsevier, 2007.

[21] J. A. Jensen, "Medical ultrasound imaging," *Progress in Biophysics and Molecular Biology*, vol. 93, pp. 153–165, 1 2007.

[22] T. Costa, C. Shi, K. Tien, J. Elloian, F. A. Cardoso, and K. L. Shepard, "An integrated 2d ultrasound phased array transmitter in cmos with pixel pitch-matched beamforming," *IEEE Transactions on Biomedical Circuits and Systems*, vol. 15, pp. 731–742, 8 2021.

[23] H. Hu, Y. Ma, X. Gao, D. Song, M. Li, H. Huang, X. Qian, *et al.*, "Stretchable ultrasonic arrays for the three-dimensional mapping of the modulus of deep tissue," *Nature Biomedical Engineering 2023*, pp. 1–14, 5 2023.

[24] V. Pashaei, P. Dehghanzadeh, G. Enwia, M. Bayat, S. J. Majerus, and S. Mandal, "Flexible body-conformal ultrasound patches for image-guided neuromodulation," *IEEE Transactions on Biomedical Circuits and Systems*, vol. 14, pp. 305–318, 4 2020.

[25] J. Elloian, J. Jadwiszczak, V. Arslan, J. D. Sherman, D. O. Kessler, and K. L. Shepard, "Flexible ultrasound transceiver array for non-invasive surface-conformable imaging enabled by geometric phase correction," *Scientific Reports 2022 12:1*, vol. 12, pp. 1–12, 9 2022.

[26] C. Seok, O. Adelegan, A. O. Biliroglu, F. Y. Yamaner, and O. Oralkan, "A 2d ultrasonic transmit phased array based on a 32x32 cmut array flip-chip bonded to an asic for neural stimulation," *IEEE International Ultrasonics Symposium, IUS*, vol. 2020-September, 9 2020.

[27] Y. Yang, H. Tian, B. Yan, H. Sun, C. Wu, Y. Shu, L. G. Wang, and T. L. Ren, "A flexible piezoelectric micromachined ultrasound transducer," *RSC Advances*, vol. 3, pp. 24900–24905, 11 2013.

[28] X. Wang, Z. Liu, and T. Zhang, "Flexible sensing electronics for wearable/attachable health monitoring," *Small*, vol. 13, p. 1602790, 7 2017.

[29] S. Wang, Y. Bai, and T. Zhang, "Materials, systems, and devices for wearable bioelectronics," *Wearable Bioelectronics*, pp. 1–48, 1 2019.

[30] H. Hu, X. Zhu, C. Wang, L. Zhang, X. Li, S. Lee, Z. Huang, R. Chen, Z. Chen, C. Wang, Y. Gu, Y. Chen, Y. Lei, T. Zhang, N. H. Kim, Y. Guo, Y. Teng, W. Zhou, Y. Li, A. Nomoto, S. Sternini, Q. Zhou, M. Pharr, F. L. D. Scalea, and S. Xu, "Stretchable ultrasonic transducer arrays for three-dimensional imaging on complex surfaces," *Science Advances*, vol. 4, 3 2018.

[31] R. F. Schaller, M. A. Melia, and F. Bocher, "Review of polymer mems micromachining," *Journal of Micromechanics and Microengineering*, vol. 26, p. 013001, 11 2015.

[32] "Which transducer type is best for ultrasonic fingerprint sensing: Cmut, pmut or pzt? — onscale." Accessed: 2023-4-9.

[33] Y. Qiu, J. V. Gigliotti, M. Wallace, F. Griggio, C. E. Demore, S. Cochran, and S. Trolier-McKinstry, "Piezoelectric micromachined ultrasound transducer (pmut) arrays for integrated sensing, actuation and imaging," *Sensors 2015, Vol. 15, Pages 8020-8041*, vol. 15, pp. 8020–8041, 4 2015.

[34] S. Smaranika Dani, Alekhika Tripathy, and N. Rao Alluri, "A critical review: the impact of electrical poling on the longitudinal piezoelectric strain coefficient," *Materials Advances*, 2022.

[35] B. E. Treeby and B. T. Cox, "k-wave: Matlab toolbox for the simulation and reconstruction of photoacoustic wave fields," *https://doi-org.tudelft.idm.oclc.org/10.1117/1.3360308*, vol. 15, p. 021314, 3 2010.

[36] "A review of conventional beam characteristics." https://www.olympus-ims.com/en/ndt-tutorials/transducers/characteristics/. Accessed: 2023-7-9.

[37] S.-C. Wooh and Y. Shi, "Optimization of ultrasonic phased arrays," *Review of Progress in Quantitative Nondestructive Evaluation*, pp. 883–890, 1998.

[38] A. Gefen, N. Gefen, Q. Zhu, R. Raghupathi, and S. S. Margulies, "Age-dependent changes in material properties of the brain and braincase of the rat," *Journal of Neurotrauma*, vol. 20, pp. 1163–1177, 2003.

[39] K. Lou, S. Granick, and F. Amblard, "How to better focus waves by considering symmetry and information loss," *Proceedings of the National Academy of Sciences of the United States of America*, vol. 115, pp. 6554–6559, 6 2018.

[40] D. Kybartas and A. Lukoševičius, "Analysis of coupled vibration modes in piezoelectric disks," *Ultragarsas / Ultrasound*, vol. 53, pp. 31–36, 12 2004.

APPENDIX I
ADDITIONAL INFORMATION ABOUT THE METHODS AND MATERIALS

A. Minimum radius of curvature

It is beneficial to decrease the kerf (i.e., spacing between PZT elements) as much as possible since this increases the total area of the piezoelectric material, which in turn enables more output pressure. Thus, the kerf must be infinitesimal to achieve a maximal active area. However, this is practically impossible because dicing blades have a certain minimal size. Moreover, when a flexible array bends too much, the top of the PZT elements will touch. This limits bending any further and might damage the PZT elements. So, decreasing the kerf in flexible arrays will increase the array's minimum bending radius (r). As depicted in figure [input], the kerf (k') at the top of the elements must be > 0 to prevent the elements from touching. The k' for a given PZT_w, PZT_{th} and r can be calculated using 6 [25]. Using this equation, the minimum bending radius r for an array so the elements don't touch can be calculated.

$$k' = \frac{1}{r}\sqrt{(\frac{PZT_w^2}{4} + (r - PZT_{th})^2)}(k - 2r * \arctan(\frac{0.5PZT_w}{r - PZT_{th}})) \tag{6}$$

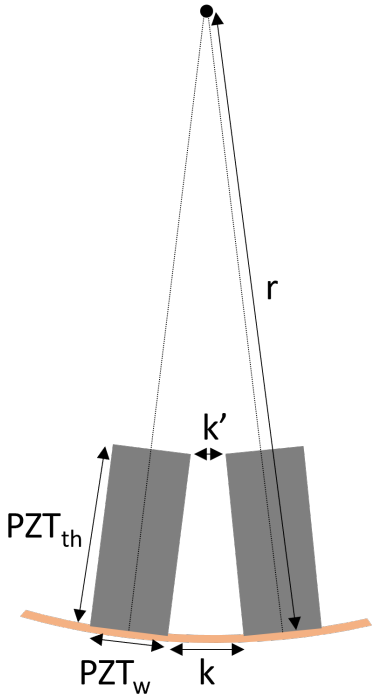

Fig. A.1: Flexible arrays have a minimum bending radius so the tops of PZT elements don't touch (k'> 0). PZT_w = PZT element width, PZT_{th} = PZT element thickness, k = kerf at the bottom of the elements, or spacing between PZT elements, k' = kerf at the top of the element, and r = bending radius.

B. Test structures

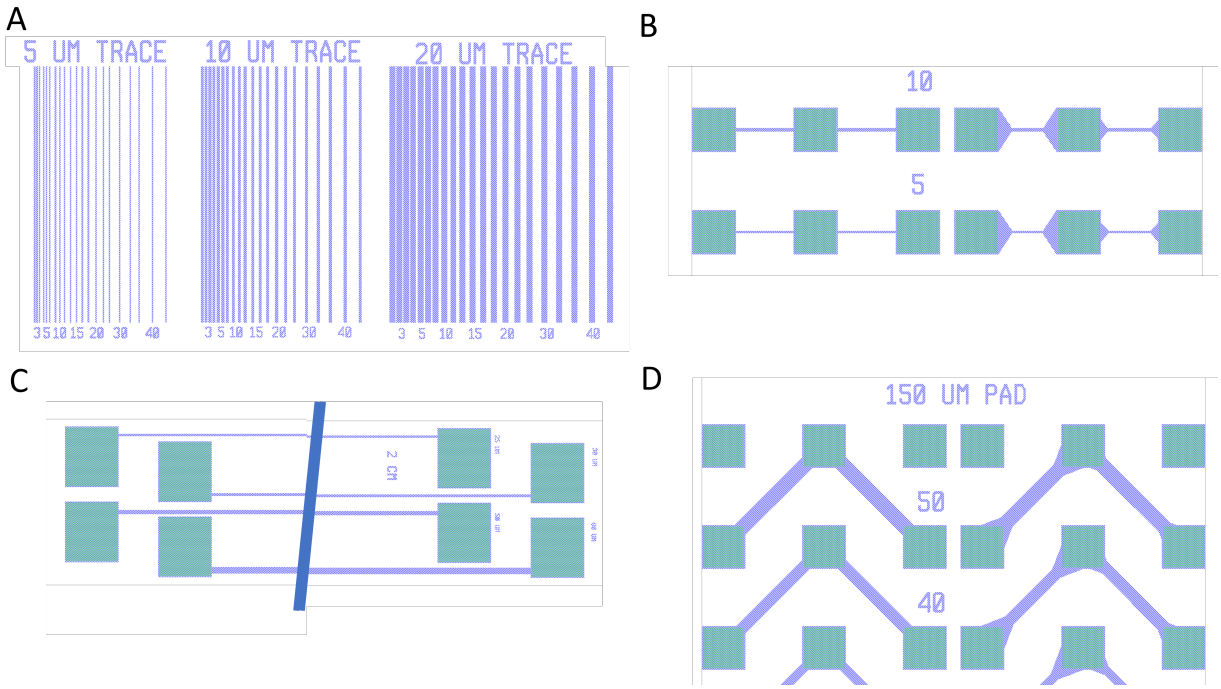

Fig. A.2: Selection of lithography mask layouts for various test structures that were used to investigate the minimum viable dimensions for the interconnecting traces. A: 1 cm long interconnecting traces with varying widths (indicated on top) and spacings (indicated at the bottom). B: Contact pads with varying edge lengths (50, 150, and 300 μm) and varying interconnecting traces, with either a tapered or straight transition from trace to contact pad. C: 2cm long traces with width varying from 5-80 μm ending in large pads to measure the resistance over the trace. D: similar as B, but with diagonal traces.

C. CAD models

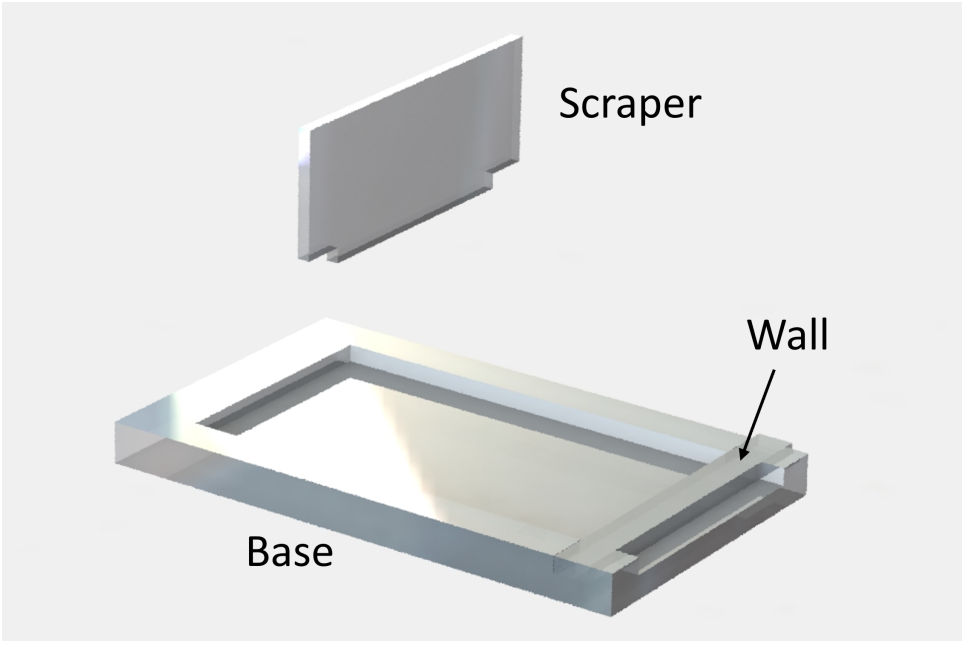

Fig. A.3: CAD moldel of the open mold for PDMS encapsulation. The scraper was used to precisely deposit a 200 μm layer in the base on which the device was placed. Then, the mold was filled entirely, and excess PDMS was removed with a blade, planarizing the surface simultaneously. Once cured, the wall was removed to ease the removal of the device from the mold.

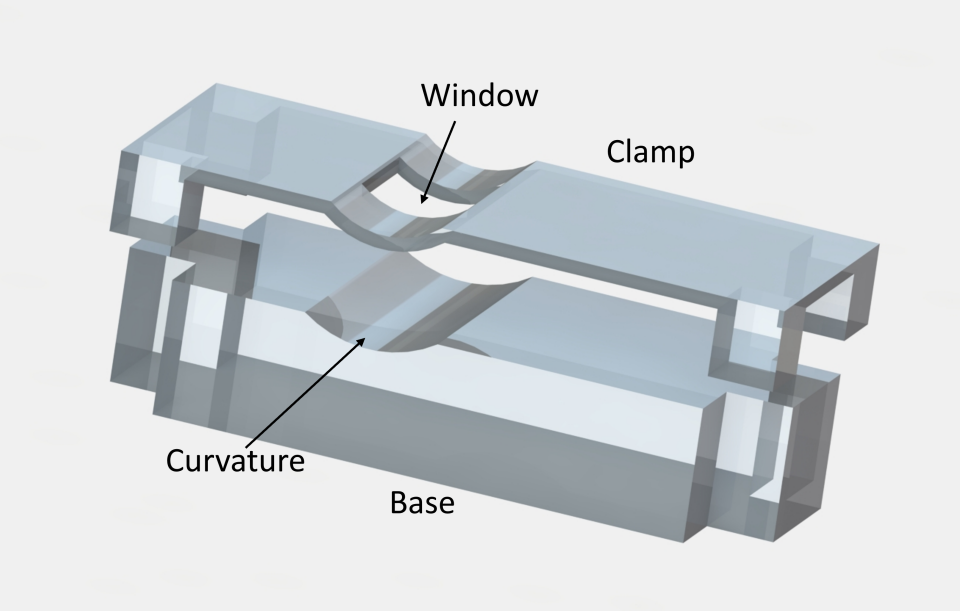

Fig. A.4: CAD model of the curved holder. The device was clamped between the base and the clamp. For US measurements in bent state, the transmitter array was placed precisely underneath the window while conforming to the 8.8 mm radius curvature.

D. Ultrasound characterization.

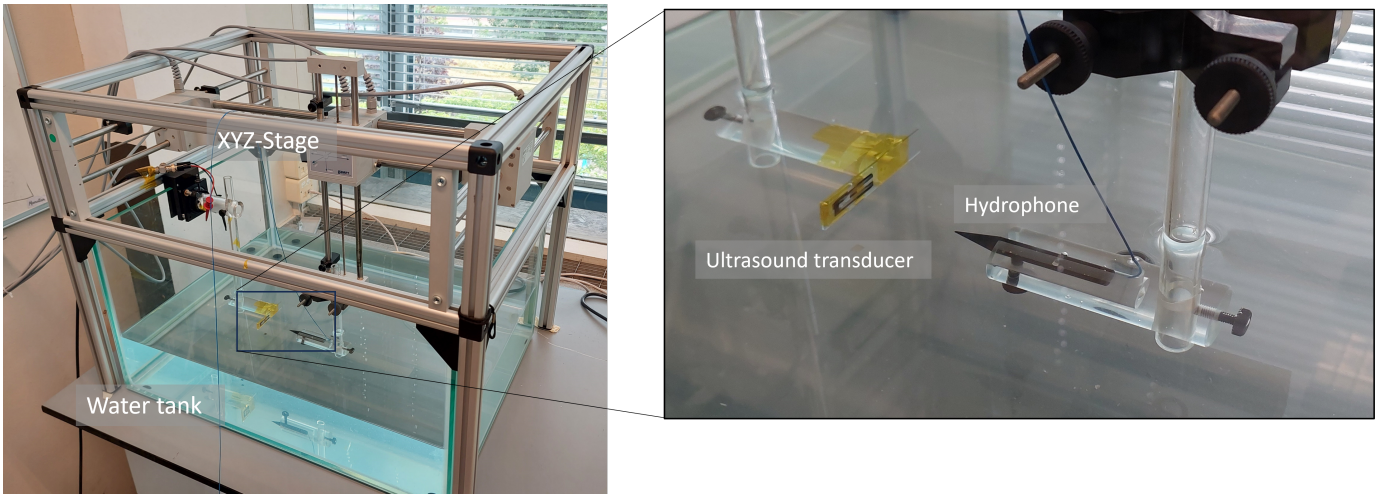

Fig. A.5: Ultrasound characterization measurement setup. The ultrasound transducer is connected to the function generator and placed inside the water tank. A computer-controlled XYZ-stage moves the hydrophone in a programmed measurement plane.

APPENDIX II
ADDITIONAL RESULTS

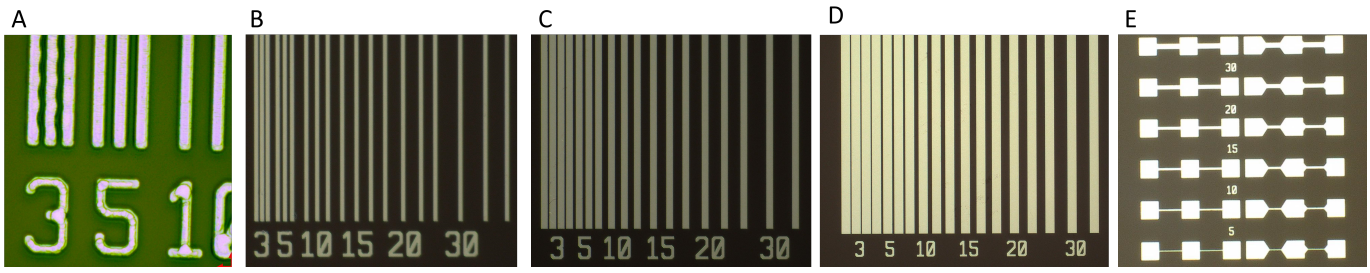

Fig. A.6: Selection of pictures showing the results of experimental metal deposition on polyimide substrate. A: 3 μm spacing resulted in a wavy pattern of the metal traces in some (not all) samples. It was deemed necessary to increase the spacing to above 3 μm. B: 5 μm traces, with spacing indicated. C: 10 μm traces, with spacing indicated. D: 20 μm traces, with spacing indicated. E: Varying trace width (indicated in μm). Transition into pads, either straight or tapered.

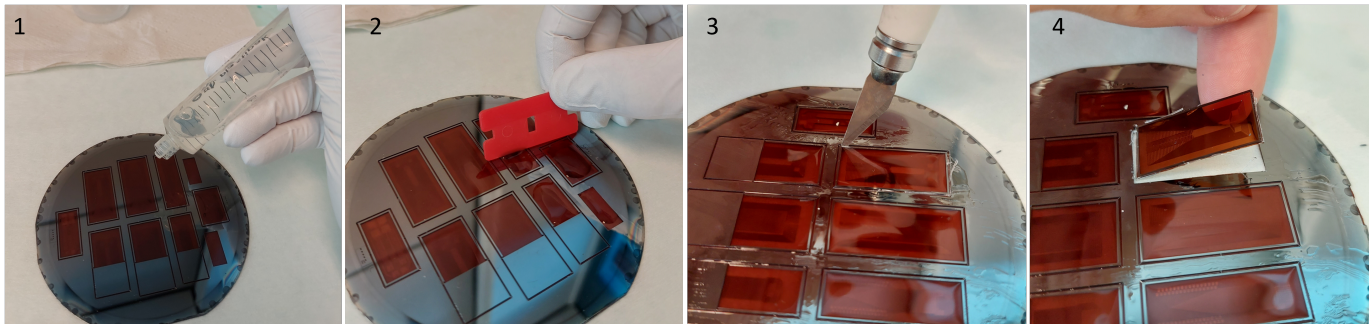

Fig. A.7: The process to release a device from the wafer. 1: PDMS was injected into the 300 μm deep cavities etched in the backside of the wafer by DRIE. 2: The PDMS is planarized with a blade and partially cured on a hotplate. 3: The polyimide and PDMS are carefully cut using a scalpel. 4: The device is released from the wafer, leaving a tiny silicon frame in place to provide support during the PZT integration steps.

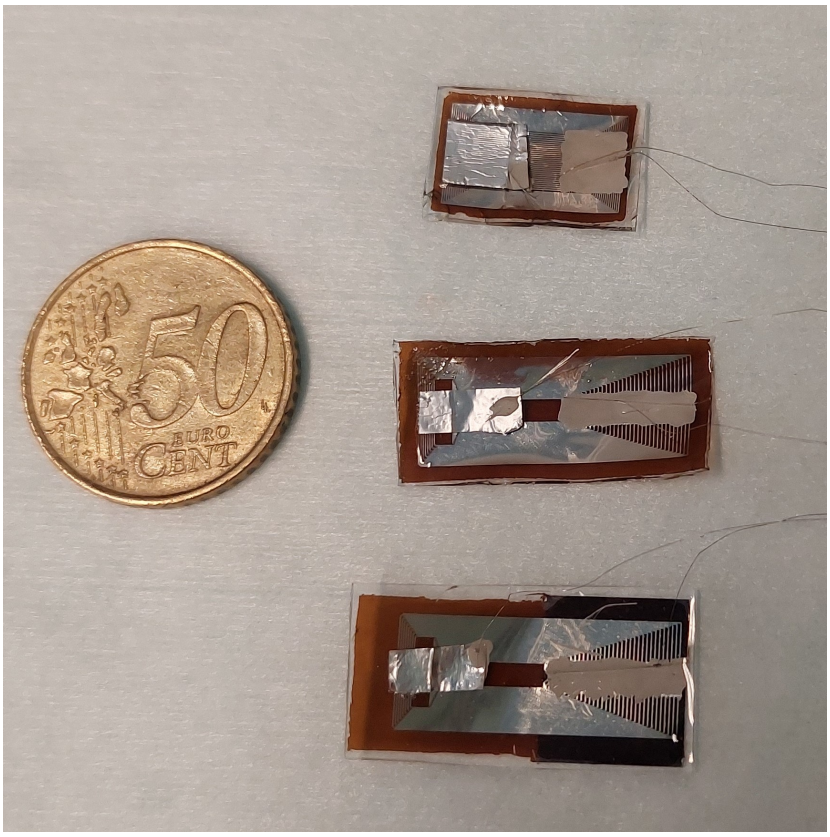

Fig. A.8: Three fully assembled devices 4 MHz flexible ultrasound transducers. From top to bottom: fully flexible 30x30 array, fully flexible 16x16 array, and flexible 16x16 transmitter array combined with a rigid contact pad array.

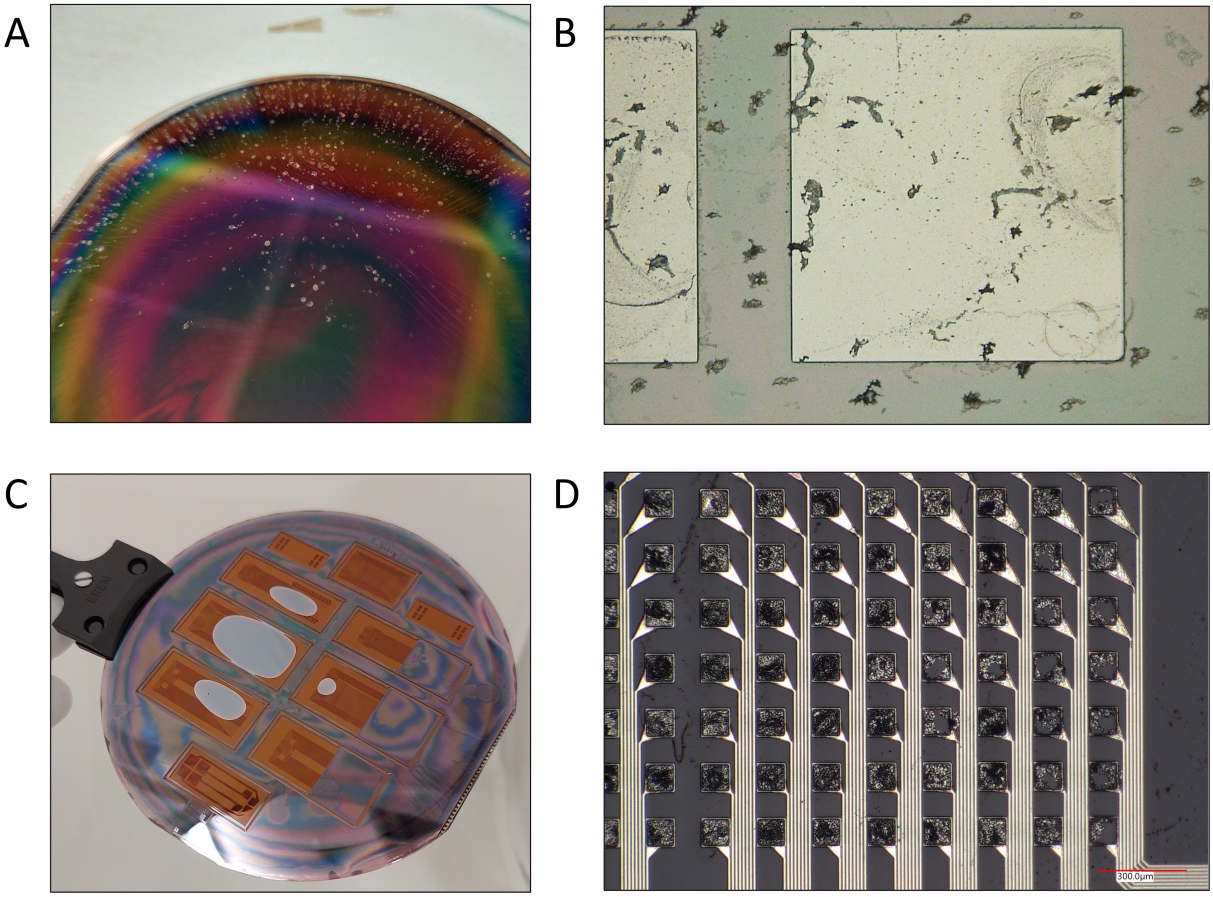

Fig. A.9: Some microfabrication difficulties that were encountered. A: Deep reactive ion etching (DRIE) on a carrier wafer resulted in insufficient cooling of the process wafer by the helium backflow. The heat led to cracks in the SiO_2 landing layer and polyimide substrate. Moreover, at higher temperatures, the selectivity of the etching process goes down, resulting in the etching of the photoresist mask. B: Underdevelopment of the polyimide insulation layer. Here, a single-puddle development process was used, which resulted in many polyimide residues. In the current process, the wafer is submerged in the developing chemicals, overcoming this problem. C: non-uniformity of DRIE. Due to different etch rates across the wafer, some cavities are not completely etched through. The remaining silicon was removed by over-etching, emphasizing the need for a sufficient landing layer. D: Insufficient selectivity of buffered hydrofluoric acid (BHF) during the wet etching of SiO_2. Once the SiO_2 is removed, the BHF will start to etch the aluminum electrodes underneath the SiO_2, severely damaging them.

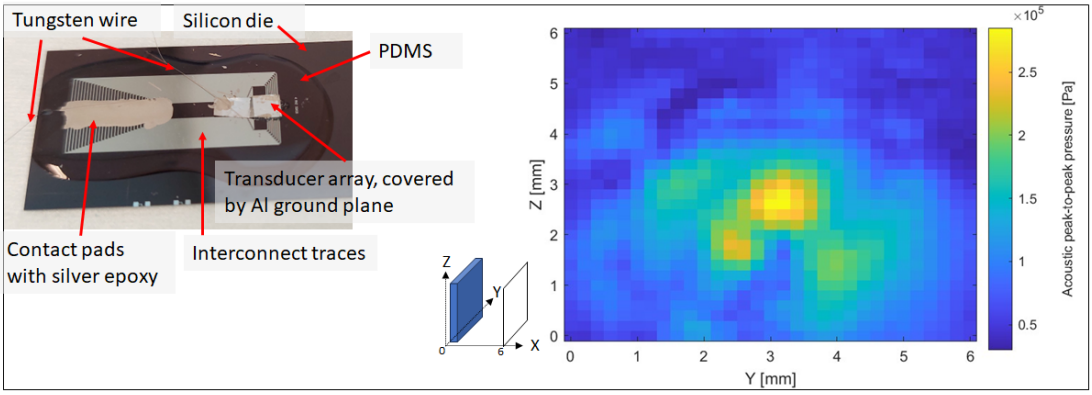

Fig. A.10: Beam profile generated by the rigid 16x16 rigid reference transducer.

Flexible Ultrasound Array

Fabrication flow chart

Process engineer:	Hidde Woerdman
Start:	January 2023
Supervisor:	Tiago Costa
Project code:	IMY I7407G
Labs:	CR100, CR10000
Contaminants:	Polymer

EKL(Else Kooi Laboratory)
DELFT UNIVERSITY OF TECHNOLOGY

Address :	Feldmannweg 17, 2628 CT Delft, The Netherlands
P.O. Box	5053, 2600 GB Delft, The Netherlands
Phone :	+31 - (0)15 - 2783868
Fax :	+31 - (0)15 - 2622163
Website :	http://ekl.tudelft.nl/EKL/Home.php

Starting Material

Use **double-sided polished wafers** with the following specifications:

Type: P-Type, boron

Wafer thickness: 300 µm

Wafer layer orientation: <100>

Wafer layer resistivity: any

Diameter: 100.0 ± 0.2 mm

Wafers taken out of an already opened box must be cleaned before processing, according to the standard procedure. Wafers taken from an unopened wafer box do not require cleaning before processing**.**
Detailed information about possible contamination:

Lab/Cleanroom	(Non-standard) material/ process steps	Process/Machine	Other materials used in the machine
CR100	Aluminium sputtering on a polymer substrate	Trikon Omega 201	Other metals
CR10000	Wet etching of SiO_2 in dedicated BHF bath.	Wet bench	

Zero layer [front side]

1. CLEANING PROCEDURE: HNO_3 100% AND 65% (IF NECESSARY)

- Cleaning. 10 minutes in fuming nitric acid (Merck: HNO_3 100%) at ambient temperature. Use the wet bench "HNO_3 (100%)" and the carrier with the red dot.
- QDR. Rinse in the Quick Dump Rinser with the standard program until the resistivity is 5 MΩ.
- Cleaning. 10 minutes in concentrated nitric acid (Merck: HNO_3 65%) at 110 °C. Use the wet bench "HNO_3 (65%)" and the carrier with the red dot.
- QDR. Rinse in the Quick Dump Rinser with the standard program until the resistivity is 5 MΩ.
- Drying. Use the Semitool "rinser/dryer" with the standard program and the white carrier with a red dot.

2. COATING AND BAKING

Use the **EVG 120 wafer track** to coat the wafers with photoresist. The process consists of treatment with HMDS (hexamethyldisilazane) vapour with nitrogen as a carrier gas, spin coating with Shipley SPR3012 positive photoresist, and a soft bake at 95ºC for 90 seconds. Always check the temperature of the hotplate and the relative humidity (48 ± 2 %) in the room first. Use recipe: **1-Co-1.4um-noEBR** (resist thickness: 1.4 µm).

3. ALIGNMENT AND EXPOSURE

Expose the wafers using the **ASM PAS 5500/80 automatic wafer stepper**. Use the following settings:
Mask: COMURK
Die size: 10x10 mm
Job: litho/fwam
Layer: 1
Exposure energy: 120 mJ/cm^2.

4. DEVELOPMENT

Use the **EVG 120 wafer track** to develop the wafers. The process consists of a post-exposure bake at 115 ºC for 90 seconds, a development step using Shipley MF322 developer (single puddle process), and a hard bake at 100 ºC for 90 seconds. Use recipe: **Dev – SP.**

5. INSPECTION: LINEWIDTH

Visually inspect the wafers through a microscope and check the line width. No resist residues are allowed.

6. PLASMA ETCHING OF ALIGNMENT MARKS

Use the **Trikon Ωmega 201** plasma etcher. Use sequence **URK_NPD** and set the platen temperature to **20 °C** to etch 1200 Å deep ASM URKs into the silicon.

7. CLEANING PROCEDURE: TEPLA + HNO_3 99%

- Plasma strip. Use the Tepla plasma system to remove the photoresist in an oxygen plasma. Use program 1: standard resist strip with endpoint detection.
- Clean the wafer for 10 minutes in concentrated nitric acid (Merck: HNO_3 99%) at ambient temperature. Use the wet bench "HNO_3 (99%) – Green metal" and the carrier for green metals.
- Rinse in the Quick Dump Rinser with the standard program until the resistivity is 5 MΩ.
- Use the Semitool "rinser/dryer" with the standard program to rinse and dry the wafers. Use the carrier for green metals.

SiO2 layer deposition [front side]

8. DEPOSIT SILICON OXIDE ON THE FRONT SIDE

Use the Novellus PECVD reactor to deposit a **10 µm thick SiO2 layer at 400 °C on the front side of the wafer.** This layer will serve as a landing layer for DRIE from the backside later in the process. A thinner layer (down to 4 µm) can be considered. Use recipe **xxxstdSiO2** with a typical deposition time of **130 sec (check log and correct deposition time if necessary)**.

9. MEASUREMENT

Use the Woolfram ellipsometer to check the SiO2 thickness.

Polyimide coating [front side]

10. SPIN COATING

Take the polyimide (Durimide 7520) out of the fridge several hours in advance to let it warm up to room temperature. Use the Brewer manual spinner to coat the wafer with a 20 µm polyimide film, following these steps:

- Dehydration bake: 2 min @150C on a hot plate. Let the wafer cool down to room temperature afterward.
- Place and center the wafer on a non-contaminated chuck.
- Pour a puddle of Durimide 7520 in the middle of the wafer.
- Run the recipe **Hidde_Durimide_20um**.
    - Spin @ 1000 rpm for 10 sec. Ramp 500/sec.
    - Spin @ 2000 rpm for 45 sec. Ramp 500/sec.
- Remove any residues from the backside with a cotton swab and acetone.
- Soft bake @ 100 °C for 3 min on a hot plate. Ramping up from a lower temperature can help to reduce bubble formation. Skipping the soft bake and placing the wafer directly in the KOYO for curing is also possible.

11. CURING

Use the KOYO oven to cure the polyimide film under nitrogen flow. The film will shrink by approximately 50%, producing a ~10 µm film. Use **program 6.**

- 2 hour ramp up to 350 °C (3 to 6 °C/min)
- Hold at 350 °C for 60 min
- 2-hour ramp down to room temperature

Close-couple the following steps: directly continue after removing the wafers from the oven.

Metal contact pads and traces [front side]

12. OXYGEN PLASMA TREATMENT

Use the Tepla oxygen plasma stripper to roughen the surface in a short, low-power oxygen plasma. Use **program 02: 1 min plasma flash @600W.**

13. METAL DEPOSITION

Use the **TRIKON SIGMA 204 sputter coater** for the deposition of metal traces. A **Leak-Up Rate (LUR)** test must be performed before sputtering. LUR must be < 2*10^-6 Torr.l/sec. Perform a **target clean at room temperature and low power**. Deposit Aluminium (99%)/Silicon(1%) 500nm at 25C with low power. Recipe: **AlSi_500nm_25C_1kW.** Visual inspection: The metal layer must look shiny.

14. COATING AND BAKING

Use the **EVG 120 wafer track** to coat the wafers with photoresist. The process consists of treatment with HMDS (hexamethyldisilazane) vapor with nitrogen as a carrier gas, spin coating with Shipley SPR3012 positive photoresist, and a soft bake at 95ºC for 90 seconds. Always check the temperature of the hotplate and the relative humidity (48 ± 2 %) in the room first. Use recipe: **SpeCo – 3012-1,4µm – No EBR**(resist thickness: 1.400 µm).

15. ALIGNMENT AND EXPOSURE

Use the **SUSS MicroTec MA/BA8 Mask aligner** to expose the wafers. Use the mask: **1 inverse – metal.** Calculate the exposure time by consulting the contact aligner exposure energy data log. Exposure energy: 120 mJ/cm^2. Typical exposure time: **7 sec (check log and correct deposition time if necessary)**.

16. DEVELOPMENT

Use the **EVG 120 wafertrack** to develop the wafers. The process consists of a post-exposure bake at 115 ºC for 90 seconds, followed by a development step using Shipley MF322 developer single puddle process. Always check the temperature of the hotplates first. Use recipe**: program Dev – SP – No Hard Bake.**

17. PLASMA ETCHING OF ALUMINIUM

Use the **Trikon Ωmega 201** plasma etcher to dry etch the aluminum. Set the platen temperature to **25 °C.** Use recipe: **AL05_350.**

18. PHOTORESIST REMOVAL AND CLEANING

A non-standard photoresist removal is necessary since a high-power oxygen plasma will etch the polyimide. Use the following steps to remove the photoresist. Repeat if necessary.

- Plasma strip
  - Use the Tepla oxygen plasma stripper to roughen and activate the surface of the photoresist. Use **program 02: 1 min plasma flash @600W**
- Cleaning
  - Use different beakers for Acetone – IPA – DI water
  - Submerge the wafer in acetone for 2 min. Agitate the beaker during this time.
  - Remove the wafer and immediately rinse with IPA.
  - Submerge the wafer in IPA for 1 min. Agitate the beaker during this time.
  - Rinse with DI water.
  - Use a Single wafer dryer - SPIN 150 to dry the wafers.

Polyimide insulation layer and contact openings [front side]

19. SPIN COATING

Take the polyimide (LTC9305) out of the fridge several hours in advance to let it warm up to room temperature. Use the Brewer manual spinner to coat the wafer with a ~3 µm negative-acting polyimide film, following these steps:

- Dehydration bake 2 min @150C. Let the wafer cool down to room temperature afterward.
- Place and center the wafer on a non-contaminated chuck.
- Pour a puddle of LTC9305 in the middle of the wafer.
- Run the recipe **Hidde_LTC_3000rpm**.
  - Spin @ 1000 rpm for 10 sec. Ramp 500/sec.
  - Spin @ 3000 rpm for 30 sec. Ramp 500/sec.
- Remove any residues from the backside with a cotton swab and acetone.
- Soft bake @ 100 °C for 2 min on a hot plate.

20. ALIGNMENT AND EXPOSURE

Use the **SUSS MicroTec MA/BA8 Mask aligner** to expose the polyimide. Use the mask **2 inverse.**
Calculate the exposure time by consulting the contact aligner exposure energy data log. Exposure: I-line 400 mJ/cm^2. Typical exposure time: **60 sec (check log and correct deposition time if necessary)**.

21. MANUAL DEVELOPMENT

Use the fume hood in the polymer lab to manually develop the polyimide so contact openings are created. Follow these steps:

- Perform post-exposure bake on a hotplate: 60 seconds @ 50 °C.
- Submerge the wafer in HTR-D2 for 90 seconds. Agitate the beaker during this time.
- Rinse with in RER-600.
- Submerge in RER-600 for 90 seconds. Agitate the beaker during this time.
- Rinse with DI water.
- Use a Single wafer dryer - SPIN 150 to dry the wafers.

22. CURING

Use the KOYO oven to cure the polyimide film under nitrogen flow. The film will shrink by approximately 50%, producing a ~1.5 µm film. Use **program 6.**

- 2 hour ramp up to 350 °C (3 to 6 °C/min)
- Hold at 350 °C for 60 min
- 2-hour ramp down to room temperature

Close-couple the following steps: directly continue after removing the wafers from the oven.

23. DESCUM OXYGEN PLASMA TREATMENT

Use the Tepla oxygen plasma stripper to remove small polyimide particles that were left behind during development. Use **program 02: 1 min plasma flash @600W**

SiO2 layer deposition [front side]

24. DEPOSIT SILICON OXIDE ON THE FRONT SIDE

Use the Novellus PECVD reactor to deposit a **200 nm thick TEOS layer at 300 °C on the front side of the wafer.** Use recipe **TEOS300** with a typical deposition time of **6 sec (check log and correct time if necessary)**.

Backside DRIE openings [back side]

25. HDMS TREATMENT

Use **EVG 120 wafertrack** for an HDMS treatment on the **backside**. This will result in better photoresist adhesion. Use recipe **Only HDMS** on the developer track.

26. COATING AND BAKING

Use the Brewer manual spinner to coat the wafer with a ~12 µm positive photoresist film, following these steps:

- Place and center the wafer on a non-contaminated chuck, with the **backside facing up**.
- Pour a puddle of **AZ12XT-20** in the middle of the wafer.
- Run the recipe **AZ12XT_12um**.
- Remove any residues from the backside with a cotton swab and acetone.
- Soft bake @ 110 °C for 3 min on a hot plate.

27. ALIGNMENT AND EXPOSURE ON THE BACKSIDE

Use the SUSS MicroTec MA/BA8 Mask aligner to expose the photoresist on the backside of the wafer. Use recipe **front-to-back alignment with soft contact**. Use mask **3 normal - backside opening.** Calculate the exposure time by consulting the contact aligner exposure energy data log. Exposure dose: I-line @ 110 mJ/cm^2 . Typical exposure time: **50 sec (check log and correct time if necessary).**

28. MANUAL DEVELOPMENT ON THE BACKSIDE

Use the fume hood in the polymer lab.

- Post-exposure bake @ 90 °C for 60 seconds on a hotplate.
- Develop in Shipley MF322 using 2 x 60 second puddles.
- Rinse with DI water.
- Use a Single wafer dryer - SPIN 150 to dry the wafers.
- Hard bake @115 °C for 3 min on a hot plate.

29. DRIE OF SILICON ON THE BACKSIDE

Use the **Rapier DRIE** to etch the silicon from the **backside**. Use the Dektak profilometer to inspect the etching depth. Target Si etch depth: 300 um. The etch rate is ~2 µm/loop at 20 °C. Perform reactor cleaning at 20 °C.
Recipe name: EKL_FlatBottom_20C
Number of cycles: 175

Wet etching of silicon oxide [both sides]

30. WET ETCHING OF SILICON OXIDE ON BOTH SIDES

Use the wet bench in CR10.000. Use neoprene gloves when handling the chemical bottle. Pour BHF 1:7 in a Teflon container. Pipet a puddle of BHF on the backside of the wafer inside the etched cavities to remove the SiO_2 landing layer. The etch rate of PECVD SiO2 in BHF is 250-300 nm/min. Calculate the required etch time and add 10% over-etch time. Rinse thoroughly in DI water for 5 min. Place the wafer in a Teflon wafer carrier. Submerge the wafer in the **BHF bath for 1 min** to remove the 200 nm PECVD TEOS on the front side. Rinse thoroughly in DI water for 5 min. Use a Single wafer dryer - SPIN 150 to dry the wafers.

Device assembly and packaging

Wafer samples will be transported outside of the cleanroom. A PZT ultrasound transducer element will be installed on the device using the pick-and-place tool in the MEMS lab. The entire device will be encapsulated in PDMS.